

IIT BHUBANESWAR

SCHOOL OF BASIC SCIENCES

PHYSICS PROJECT REPORT

MODELLING OF ION BEAM MODIFIED NANOWIRES USING COARSE-GRAINED MOLECULAR DYNAMICS SIMULATIONS

Author:

Souvik CHAKRABORTY
18PH05013

Supervisors:

Dr. Shyamal CHATTERJEE
Dr. Hemant KUMAR

April 12, 2025



IIT Bhubaneswar

Indian Institute of Technology Bhubaneswar

Contents

| | | |
|----------|--|-----------|
| 1 | Introduction | 1 |
| 1.1 | Literature Review | 1 |
| 1.2 | Aim of the Research | 5 |
| 2 | Introduction to Molecular Dynamics Simulations | 6 |
| 2.1 | The Basics of Molecular Dynamics simulations | 6 |
| 2.1.1 | Non-reactive force fields | 7 |
| 2.1.2 | Integrators in Molecular Dynamics | 7 |
| 2.1.3 | Optimization of the simulation | 8 |
| 2.1.4 | Thermodynamic Ensembles | 9 |
| 3 | Methodology | 11 |
| 3.1 | Tools and programs | 11 |
| 3.1.1 | For Molecular Dynamics Simulations | 11 |
| 3.1.2 | For Data Analysis | 12 |
| 4 | Some Basic Simulations to Get Started | 15 |
| 4.1 | Simulation of Copper lattice | 15 |
| 4.2 | Simulation of Biomolecules | 17 |
| 5 | Simulation and Results | 21 |
| 5.1 | Simulating Nanowires with a Hundred Pseudo-atoms per Chain | 21 |
| 5.1.1 | Modelling the nanowires | 21 |
| 5.1.2 | simulation process | 22 |
| 5.1.3 | Simulation of ion-beam radiation | 22 |
| 5.1.4 | Comparison and Results: | 23 |
| 5.1.5 | Variation with temperature | 25 |
| 5.2 | Simulating Nanowires with a Thousand Pseudo-Atoms per chains | 25 |
| 5.2.1 | Coarse-Grain Modelling the Nanowires | 25 |
| 5.2.2 | Simulating the Nanowires | 26 |
| 5.2.3 | Simulating the Ion-Beam Irradiation Process | 27 |
| 5.2.4 | Analysis and Results | 28 |
| 5.3 | Conclusion | 29 |

Abstract

Batteries have been accepted as the primary electrical energy storage device with Lithium Ion Batteries (LIBs), developed in 1991, being the most widely used batteries in portable devices. However, in order to meet future demands, batteries with higher energy density and higher power density are required. Experimental results suggest that the performance of LIBs and other electrical energy storage devices can be highly enhanced by replacing conventional electrodes with modified one-dimensional nanowires. Ion beam irradiation is an accepted method of modifying nanowires which can introduce both chemical and physical changes to the irradiated material. In this project, we investigate the effects of ion beam irradiation on the surface properties of nanowires of two different lengths (one with 100 beads per chain and the other with 1000 beads per chain) using Coarse-Grained Molecular Dynamics (CGMD) simulations, and analyse its effectiveness in the development of high performance electrode materials. We start with a 10×10 array of rigid and pristine nanowires and then introduce minor bends to the system to replicate the effects of low-fluence irradiation. Then we allow the formation of bonds between the wires to introduce the effects of high-fluence irradiation. Finally, we compare the unmodified and the modified systems to investigate the changes introduced via the irradiation method. Results reveal a moderate increase in the solvent accessible surface area (SASA) for the shorter nanowires whereas a minor decrease in the surface area for the longer nanowires after the irradiation process, compared to their unmodified counterparts. This suggests the existence of an optimum length for which the irradiation process can be effective in increasing the capacity of the nanowires. Further investigation needs to be conducted to find this optimum length for different nanowire systems.

Chapter 1

Introduction

1.1 Literature Review

Batteries and electrochemical capacitors have proved to be extremely useful electrical energy storage devices with Lithium-Ion batteries being the most widely used energy storage device when it comes to portable appliances[1][2]. Batteries have gained widespread popularity due to its portability, long life span, low maintenance, high energy (in case of primary batteries) and power (in case of secondary batteries) densities as well as several other factors. A typical battery consists of a number of electrochemical cells connected in series (to obtain high voltage) or in parallel (to obtain high current). Electrochemical cells mainly consists of three parts- the anode, the cathode and the electrolyte; and converts chemical energy directly to electrical energy.

The anode is the negative electrode which donates electrons to the external load/circuit during the discharge process and gets oxidized during the process. The efficiency of an anode depends on its quality as an oxidizing agent, conductivity, Coulombic output (Ah/g) and stability. Metals such as Zinc and lithium have been widely adopted as anodes. Cathodes on the other hand are the positively charged electrodes which accepts the electrons from the external circuit during discharging and are chosen based on their reducing properties and stability. The most commonly used cathodes are metal oxides. The electrolyte acts as a medium to transport the charges. Electrolytes can be liquid or solid with preferably high ionic conductivity and must be chemically inert to the electrodes.

Based on the reusability, electrochemical cells can be classified into two classes: primary and secondary cells. The primary cells are non-rechargeable and have high energy densities and moderate discharge rates. The secondary cells are rechargeable and offers high power densities with very good discharge rates.

The maximum amount of obtainable energy from the battery depends on the nature of the active materials which in turn determines the voltage whereas the amount of the active materials determines the Coulombic capacity i.e, the Ampere-hour capacity. However, in reality the actual energy obtained is much lesser than the expected value due to the presence of the electrolyte and several non-reacting materials. As a result, the performance of cells is generally expressed as a ratio of the energy output to its weight which is known as specific energy or to its volume, in which case is it known as the energy density. While batteries are popular for their high energy density, electrical double-layered capacitors and pseudocapacitors are the usual choices when high power density is required. However, both conventional batteries and capacitors have their share of disadvantages which can limit their performances. There is a constant demand for higher power and energy, higher rate performance, greater life span and less charging time in energy storage devices, which indicates the requirement of a better alternative for storing energy. As a result, there have been numerous attempts to replace the conventional electrodes used in such devices with materials capable of delivering the above-mentioned qualities.

Recent advances in Nanotechnology has provided us with a variety of novel technologies and has also contributed to the search for better energy storage devices. Low dimensional materials, especially one-dimensional nanowires or nanorods, have a wide range of properties which makes them potential candidates for high-performance electrodes. The first key advantage of implementing nanowire electrodes is their high surface to body ratio, which increases the contact area between

the electrolyte and the electrode, thus increasing the utilization of active materials and the rate performance of the device[3][4][5]. The next advantage is that nanowires, due to their geometry are highly resistant towards volumetric strain, which means the density of the active materials can be increased to achieve better energy density without suffering from mechanical degradation[6][7][8]. This is in contrast to the widely used Lithium-ion batteries which get easily damaged by volume expansion. Nanowires can also be easily grown on a metal or carbon surface without requiring any binding agent. As a result they can provide direct pathways for electric transport unlike nanoparticles[9][6][10][11]. Moreover, nanowires have a shorter diffusion length compared to their bulk counterpart providing a shorter ion transport pathway which decreases the characteristic time and increases the rate of charging/discharging[9][12][4][13][14]. They can also be used as building blocks for making complex branched and hierarchical architectures[15][16][17][18]. There are several studies conducted which acknowledges the necessities of nanowires in making energy storage devices[19][20][21][5][22][23][24].

As mentioned earlier, the consumer markets for batteries have been dominated by Lithium-Ion batteries since 1991. This is due to their comparatively higher energy density, cost efficiency and long life cycle. However, its gradual capacity decay, resulting from the loss of Li ions during the charging/discharging period, limits its use for future applications[25]. To meet this increasing demand for storage devices with even higher energy density, power density and capacity, nanowire electrodes are being extensively studied for their unique aforementioned properties. The fact that nanowires are inherently inert towards any volumetric change, and have large surface area, in particular, makes them a potential material for developing high performance electrodes. Silicon nanowires have emerged as a promising candidate for constructing anodes for LIBs due to certain favourable qualities[23][26]. The Silicon nanowire electrodes prepared by Chan et al.[6] have shown better charging/discharging capacity and accommodation of the volumetric changes compared to other forms of Silicon electrodes. Another material considered for developing nanowire anode is Germanium. Bulk germanium has higher Lithium diffusivity, conductivity, capacity and energy density than Si[6][27][28]. However, it suffers from large structural deformations during charging/discharging cycles which limits its usage. Germanium nanowires on the other hand, offers better resistance to such volume changes[6]. When it comes to LIB cathodes, LiCoO₂ is the most widely used material with a good theoretical capacity of 274 mAh/g. However, only half of it is reversible and can be used in rechargeable batteries [29]. This challenge can be overcome using LiCaO₂ nanowire electrodes which offers better resistance to stress or strain and faster transport pathways for Lithium-ions. However, due to its high cost and toxicity, nanowires of LiMn₂O₄, LiFePO₄ Li₃V₂(PO₄) have gained popularity as potential cathode materials. These nanowires, designed in a number of different ways, provides better capacity, rate capabilities and faster diffusion paths compared to their two and three dimensional versions[13][30][31][32][33].

Besides batteries, electrolytic supercapacitors have also emerged as effective electrical energy storage devices, which can store high energy in their electrical double layers, thus acting as a bridge between conventional batteries and dielectric capacitors. Compared to batteries, supercapacitors have significantly lower energy density but higher power density and longer life cycle. Nanowire electrodes have been highly effective in enhancing the performance of supercapacitors due to their high surface to body ratio providing greater area of contact between the electrode and the electrolyte and allowing greater number of ions to be adsorbed on the electrode surface, thus promoting the rate performance of the supercapacitors[15][34][35][36]. These nanowires also provide a faster route for the electrons further enhancing the power density and rate performance of the supercapacitors[37].

Although the unique properties of one dimensional nanowires have made them promising candidates for constructing energy storage devices, there are several challenges that have to be dealt with before they can replace the conventional electrode materials. Let us discuss some of them and the steps taken to remedy them. The Silicon nanowires developed by Chan et al.[6] provided better electrochemical performance but failed to achieve high enough mass loading for practical usage. To tackle this issue, Hu et al. constructed a three dimensional porous structure of silicon nanowires using CVD method[38]. The three dimensional construct increases the area-normalized

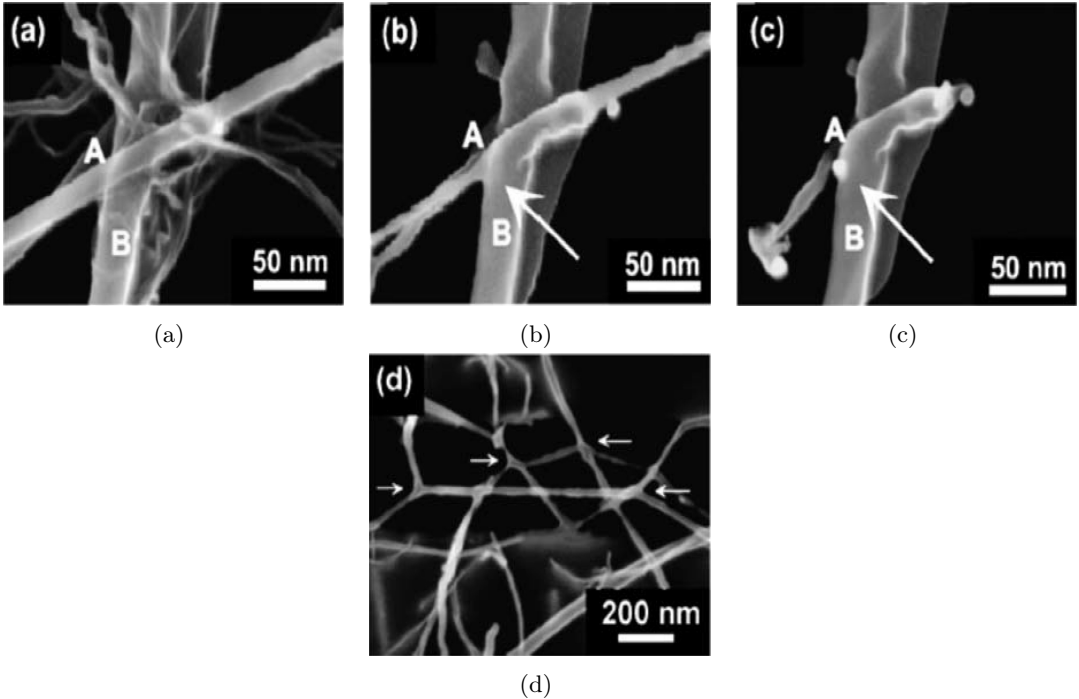


Figure 1.1: SEM images of two nanowires marked as A and B at various stages: (a) before irradiation, (b) after irradiation by 10^{16} ions/ cm^2 at 10 keV energy, (c) after irradiation by 10^{16} ions/ cm^2 at 10 keV energy. (d) SEM image of a nanowire network formed by welding due to ion-beam irradiation. The images are taken from reference [46]

specific capacity from 0.6 to 2.5 mAh Cm⁻² in comparison to the pure silicon nanowires. Another instance of modifying nanowires for making anodes was exhibited by Li et al who managed to grow silicon nanowires on stainless steel with the help of gold nanoparticle and carbon nanotubes. the hybrid system provided an even better areal capacity[39]. In addition to these, Silicon nanowires grown on lightweight carbon nanofiber film showed high mass loading and specific capacity[40][41]. Other works include construction of amorphous Si shell nanowires with carbon nanofiber as its core, where the carbon nanofibers provide electron transport pathways, high areal capacity and undergoes less volumetric changes compared to other silicon nanowire structures[17]; and construction of mesoporous nanowires which showed a sufficiently high coulombic efficiency and a high rate capacity[42]. When it comes to Germanium, nanostructured Ge provides much better structural integrity compared to bulk Ge anode, but it is difficult to establish a contact between the nanowires and the current collector. Chan et al solved this problem by growing the Germanium nanowires directly on the current collector[6]. The structure was stable even under large strain and showed high rate capacity, good cycling life and a very high coulombic efficiency. Ko et al. managed to design a heterostructure with Germanium nanowires as core and covered by Germanium suboxide layer which provided an even larger capacity of 900 mAh g⁻¹ at 1C[43].

In case of cathodes too, it has been observed that carefully modified nanowires perform better compared to the unmodified ones. For example, Jiao et al. designed both LiCoO₂ nanowires and mesoporous LiCoO₂ nanowires to compare their performances and it was observed that the mesoporous structure provided better capacity and stability than both the nanowired structure and the normal LiCoO₂ [44]. Xiao et al. designed (0 1 0) plane exposed LiCoO₂ nanowires with excellent capaciy retention, high rate performance and stability due to its geometry. Xia et al. was able to design a three dimensional mesoporous structure made of LiCoO₂ nanowires for their utilization in microbatteries[45]. The three dimensional structure wih high surface area offered much superior rate performance, gravimetric and areal capacity and stability compared to the lower dimensional nanowire structures. These type of modifications,however, are not only limited to Silicon, Germanium and LiCoO₂, but several other nanowired electrode materials have also been treated in a similar manner to further enhance their performance

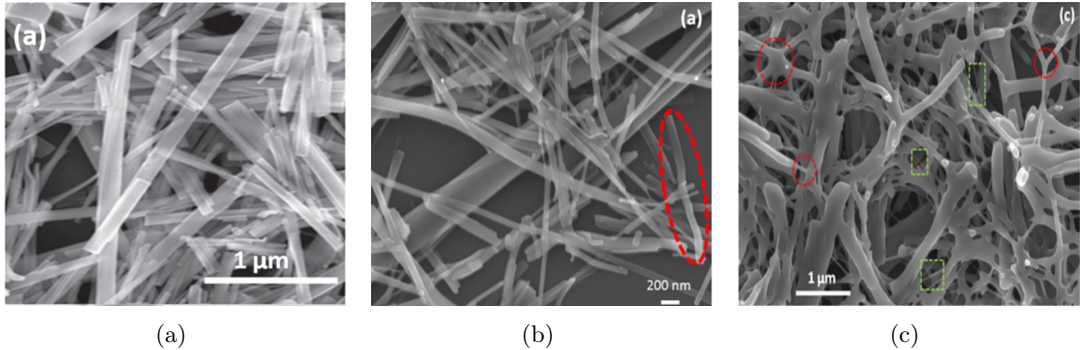


Figure 1.2: (a)SEM Plan-view of Hydrogen Titanate before irradiation. (b)Formation of junctions and bending of the nanowires observed after irradiation with 30 keV N^+ at a fluence of 5×10^{15} ions cm^{-2} (c) formation of junctions in large scale is observed after irradiation with 30 keV N^+ at a fluence of 2×10^{16} ions cm^{-2} . The images are taken from reference [49]

Similarly, nanowires adopted as electrodes in supercapacitors and pseudocapacitors have also been subjected to modifications in order to boost their performances. Carbon nanotubes and nanofibers are the main focus of interest when it comes to supercapacitor electrodes due to their high surface area and porosity, thus increasing the adsorbable area for the ions. Cross-linked carbon fibers, in addition to the above mentioned qualities, possess high structural stability and thus offers an edge over the carbon nanotubes. Doping the nanowires with foreign elements is another widely practised method of modification. Chen et al. designed Nitrogen doped carbon nanofibers with high energy density and specific capacity[47]. Metal oxides like MnO_2 nanowires are widely used as pseudocapacitors due to their excellent electrochemical performance. Xia et al. further improved on the performance of the MnO_2 nanowires by doping them with gold nanoparticles which resulted in highly increased capacitance and rate performance[48].

It is a proven fact that nanowires possess certain unique advantages which makes them a better alternative for conventional bulk electrodes. However, inspite of the extensive research carried on in this field, there are still some issues that needs to be addressed before they can be brought to the market. Most of the methods used for fabrication and enhancement of the nanowires are expensive and thus difficult to produce in a large scale. There is a need of a fabrication method which can precisely control the size and morphology of the nanowires and their architecture so that their performance can be tuned according to the needs. It has been observed that some materials are suitable as electrodes in their nanowire form but fail to perform nearly as good in their bulk form. This raises the possibility of several new materials waiting to be discovered that can serve as a high performance electrode. Ample theoretical simulations are required to discover such materials. Alongside we should also continue our search for alternative techniques for modifying nanowires for the best performance.

One of the key requirements for a good electrode is its capacity of storage. It is observed that in most of the modern batteries, the electrodes are porous. Porous electrode provide larger adsorption sites for the electrolytic ions as well as can act as a localized reservoir for the electrolytic ions and thus offer better storage capacity, better rate performance and improved mass and charge transfer. Three dimensional cross linked nanowire structures have been proven to be superior compared to the normal nanowires. Ion-beam irradiation is a tried and tested procedure for producing such porous structures[49][50]. Research has revealed that in addition to doping of semiconductors and ion beam nitriding of steel, ion beam irradiation can give rise to certain beneficial properties in case of nanowires. Experiments have confirmed that ion irradiation can alter the structure and properties of carbon nanomaterials like carbon nanotubes and graphene in a controlled manner[51][52][53][54][55][56][57][58][59][60][61]. In addition to this, it has been observed that the irradiation process often introduce changes in the mechanical[53][55], electronic[56][62][63][46][64] and magnetic[65][66] properties of nanomaterials. However, our main reason of interest in ion beam irradiation is due to its ability to interconnect and weld nanowires to produce a porous network[49][54][57][67][68]. It has been experimentally observed that both lower and higher fluence ion irradiation can give rise to junction formation. When a bunch of pristine

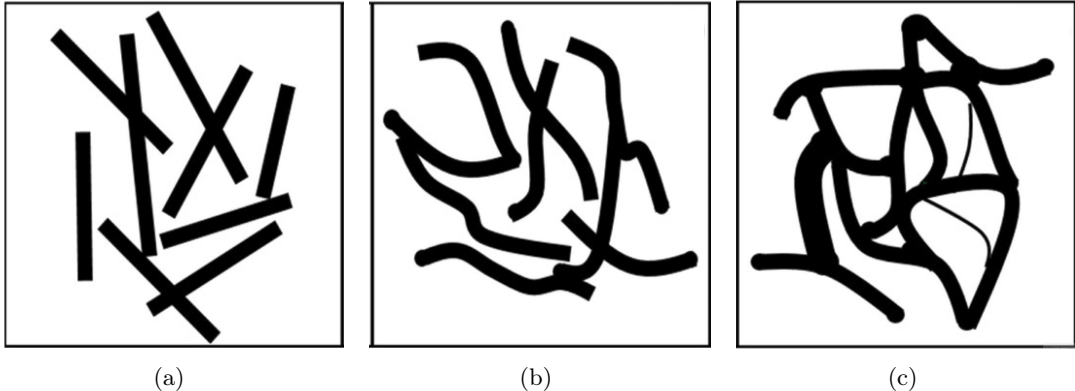


Figure 1.3: Schematic representation of nanowires during different stages of the ion-beam radiation process: (a) Pristine nanowires before the irradiation commences, (b) The nanowires start to bend and even form joints after low-fluence irradiation. (c) Large scale welding of the nanowires at higher fluence.

nanowires are subjected to ion beam irradiation at lower dose, they start bending and show signs of junction formation[55][62][69][70]. This is due to the amorphization of the nanowires which increases the bending modulus and as the bending modulus is associated with the shear modulus, the whole process gives rise to covalent bonds. Theoretical simulations have also predicted such type of bonds. On the contrary, irradiation at higher fluence, shows dramatic increase in the bond formation, giving rise to ‘X’, ‘Y’ type of bonds and large-sale junction formation[49][71][72][73][74]. This is because at higher fluence, the nanowires experiences localized melting where solid junctions are formed. This facilitates the formation of an interconnected network of nanowires.

1.2 Aim of the Research

The variation of conductivity with irradiation is controlled by two key factors: the covalent bonds produced enhances the inter-nanowire conductance whereas the amorphization of the nanowires occurring at high dose tends to decrease the conductivity. Since, electrochemistry is primarily an interfacial phenomenon, we need to understand the effect of ion-beam irradiation on the solvent accessible surface area of the nanowires in order to discover any additional effects arising from the surface area change. This is the primary focus of this paper. Here, we use Coarse-Grained Molecular Dynamics (CGMD) simulation to model the pristine nanowires and then mimic the process of ion beam irradiation and finally calculate the change in solvent accessible surface area (SASA).

Chapter 2

Introduction to Molecular Dynamics Simulations

Computer simulations act as great tools for analyzing complex realistic situations which are otherwise impossible to analyze analytically. Molecular Dynamics is one of such toolbox primarily used to tackle many-body problems using classical mechanics (Newton's law). It has found extensive use in statistical physics, physical chemistry and biophysics which deals with the interaction among a large number of particles. It helps to bridge the gap between the microscopic world of atoms and molecules and the macroscopic one which deals with the properties of the entire system. The first ever molecular dynamics simulation was done by Rahman in 1964[75]. At present, it is common to simulate systems consisting of upto 5 million atoms using molecular dynamics which has made it an extremely efficient tool for the analysis of biological systems like proteins and other large molecules. However, its use is not limited to biology only. Over the last decade Molecular dynamics have been extensively used to study different properties of one and two dimensional materials. These includes properties like thermal conductivity[76][77][78][79][5], biocompatibility[80][81][82][83] of 2D surfaces and tensile behaviour[84][85][86][87] of nanowires.

2.1 The Basics of Molecular Dynamics simulations

Molecular dynamics algorithm involves building a macroscopic model of the system in a simulation box of interest and defining the hamiltonian for the system (let's say containing N particles) in the following form:

$$H(q, p) = E_K(p) + V(q) \quad (2.1)$$

$$\begin{aligned} q &= q(q_1, q_2, q_3, \dots, q_N) \\ p &= p(p_1, p_2, p_3, \dots, p_N) \end{aligned}$$

where p and q are the generalised coordinate and the generalised momenta respectively. The usual procedure involves providing each particle in the system with some random velocity. Henceforth, the kinetic energy is calculated as;

$$E_K = \sum_{i=1}^N \sum_{\alpha=1}^3 \frac{p_{i\alpha}^2}{2m_i} \quad (2.2)$$

where i stands for the particle number and α refers to the components of the momentum along the 3 dimensions. The potential energy comprises of both the potential due to an external force (if present) and the potential arising from the different types of interactions between the particles in the system. As a result, sometimes it becomes a challenge to correctly define the potential beforehand. The most general form of the potential energy is given as;

$$V = \sum_i u_1(r_i) + \frac{1}{2} \sum_i \sum_{j>i} u_2(\mathbf{r}_i, \mathbf{r}_j) + \sum_i \sum_{j>i} \sum_{k>j>i} u_3(\mathbf{r}_i, \mathbf{r}_j, \mathbf{r}_k) \dots \quad (2.3)$$

Here u_1 is the potential of the external field, u_2 is the potential arising due to the interaction between any two atoms whereas u_3 takes into account the interaction among three atoms and so on.

These potentials are known as 'force fields' in molecular dynamics, and can be broadly classified into two categories-(a)Reactive force fields, which deals with the dynamics of chemical bond breaking and formations, primarily used to simulate chemical reactions; and (b)Non-reactive force fields, which deals with the different interactions between the particles.

2.1.1 Non-reactive force fields

For our study, we only need to focus on the non-reactive force fields, especially the van der Waal's interaction and the bonded interaction.

- **van der Waal's interaction:** The van der Waal's interaction is modelled using the 12-6 Leonard Jones potential which can be attractive or repulsive depending on the inter-atomic distance:

$$V_{LJ}(r) = 4\epsilon \left[\left(\frac{\sigma}{r} \right)^{12} - \left(\frac{\sigma}{r} \right)^6 \right] \quad (2.4)$$

Where ϵ denotes the depth of the Leonard Jones potential well in energy units, and σ denotes the inter-atomic distance where the LJ interaction becomes zero.

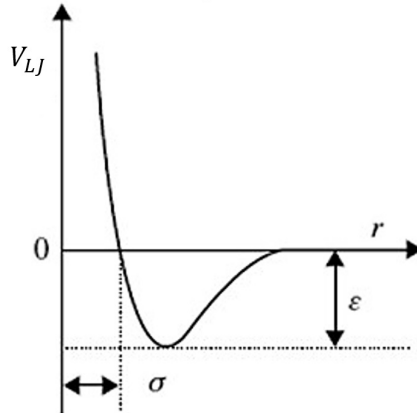


Figure 2.1: The Leonard Jones potential.

As the attractive part decays as r^{-12} for all practical purposes, we consider the cut-off of the potential at 2.5σ beyond which it is taken to be 0.

- **Bonded interactions:** These types of interactions become important when dealing with molecules which deals with the stretching of bonds and bending of angles. Usually the bond and the angle energies are modelled using harmonic potentials given by:

$$E_{bond}(r_{ij}) = \frac{1}{2}k_b(r_{ij} - r_0)^2 \quad (2.5)$$

$$E_{angle}(\theta_{ijk}) = \frac{1}{2}k_\theta(\theta_{ijk} - \theta_0)^2 \quad (2.6)$$

Here, r_0 and θ_0 represents the equilibrium distance and the equilibrium angle respectively and k_b and k_θ are the force constants of the interactions. Some of the other bond interaction types include nonlinear, finite-extensible non-linear elastic (FENE) bond etc. Similarly there are a number of available angle interaction types to choose from.

2.1.2 Integrators in Molecular Dynamics

Once the potential is defined, the next step is to solve the classical equations of motion for the particles given as:

$$m \frac{d^2\vec{r}}{dt^2} = -\nabla V \quad (2.7)$$

As a realistic system generally consists of a large of atoms, we need some algorithm to integrate the above second order differential equations to obtain the positions and velocity. Molecular Dynamics have some predefined integration schemes which helps in the process. The Verlet algorithm, the velocity-verlet algorithm[88], the leap-frog algorithm, the predictor-corrector algorithm are a few of them. However the most important one and the one relevant in our study is the Velocity-Verlet algorithm.

- **The Velocity-Verlet Algorithm:** The first step of the simulation involves defining the initial positions of all the particles in the system and assigning velocities to the particles. The velocities can be totally random or can follow a predefined distribution function. Let us consider a particle in the system whose position at time ' t ' is given by $r(t)$. Then after an interval of ' δt ' the updated position can be obtained in terms of velocity and acceleration using Taylor expansion:

$$r(t + \delta t) = r(t) + v(t)\delta t + \frac{F(t)}{m} \frac{\delta t^2}{2!} + \dots \quad (2.8)$$

Similarly, the position of the particle before an interval of ' δt ' will be:

$$r(t - \delta t) = r(t) - v(t)\delta t + \frac{F(t)}{m} \frac{\delta t^2}{2!} - \dots \quad (2.9)$$

Adding the above two equations we obtain the relation between the initial and final position as:

$$r(t + \delta t) = 2r(t) - r(t - \delta t) + \frac{F(t)}{m} \delta t^2 \quad (2.10)$$

Neglecting the higher order terms due to the small size of the timestep ' δt '. Similarly, the velocity of the particle before an interval of ' δt ' will be:

$$v(t + \delta t) = v(t) + \frac{1}{2m} [F(t) + F(t + \delta t)] \delta t \quad (2.11)$$

The algorithm first updates the position coordinates using equation (10) and then calculates the velocity coordinates at the middle of the step as

$$v(t + \frac{1}{2}\delta t) = v(t) + \frac{1}{2m} [F(t)] \delta t \quad (2.12)$$

This helps to calculate the velocity at the next timestep as:

$$v(t + \delta t) = v(t + \frac{1}{2}\delta t) + \frac{1}{2m} [F(t + \delta t)] \delta t \quad (2.13)$$

Thus an integrator can calculate the entire trajectories of particles just by having information about the forces present in the system and the positions and velocities of the particles at the beginning of the simulation.

2.1.3 Optimization of the simulation

Real system used in experiments contains a large number of molecules which are impossible to simulate within finite time using existing computational methods. One way to tackle this problem is to simulate only a part of the system in a much smaller simulation box. In order for the simulation box to mimic the characteristics of the real system, a number of optimization steps have been implemented. The two most important implementations are discussed below:

- **Periodic Boundary Conditions (PBC):** This is a simple yet effective way to preserve the original characteristics of the system in the simulation box. The boundaries along all the axes are made periodic. This prevents any unwanted interactions that can happen at the boundary edges. So when a particle leaves the box from one end, it enters from the opposite one and thus the total number of particles in the box always remains conserved. However, this also presents with a few problems. One of them is inability to calculate any fluctuation greater than the length of the simulation box. As a result the size of the box should be chosen carefully.

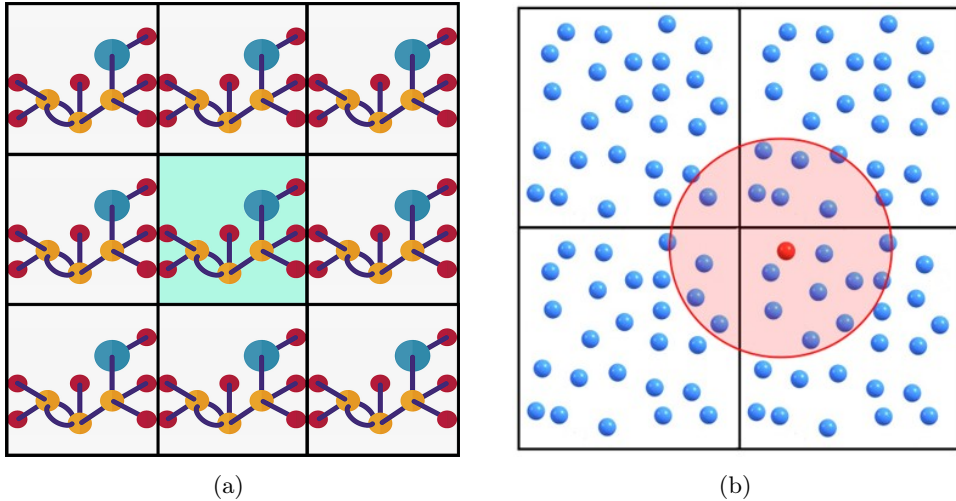


Figure 2.2: Schematic representation of the operations performed in RMSD calculation. The figure shows configurations of a simple molecule in 2D (a) initially at two different timesteps (b) when the COMs of the molecules are made to coincide. (c) when a rotation operation is performed to superpose one structure on another. After this step the RMSD can be calculated.

- **Cut-off and switching Function:** Simulating a large number of particles means calculating all the interactions among them every step. This greatly reduces the computational time. For example, simulation N number of particles requires calculation of $\frac{N(N-1)}{2}$ number of pair-wise interactions every step. For short-ranged interactions, this can be avoided using a cut-off for the interactions. This method involves defining a sphere around the particle of interest keeping in mind the periodic boundary conditions and considering particles only within that sphere only for calculation of the pairwise interactions. However, this also needs special attention so that it does not violate the rules of the system. The cut-off radius cannot be greater than half of the length of any of the sides of the simulation box. Otherwise, the same particles will be calculated twice due to the PBCs. A sudden discontinuity in the force fields makes the system unstable. This can be avoided by using a suitable switching function, which instead of abruptly ending the potential introduces a smooth transition from the finite value to 0.

2.1.4 Thermodynamic Ensembles

The above mentioned integration schemes keeps the number of particles, volume and the energy of the system constant. In other words, the integrator are good only for simulating systems in the microcanonical (NVE) ensemble. Molecular Dynamics allows simulations of systems under constant pressure and constant temperature too using barostats and thermostats respectively.

- **Constant temperature simulations:** The temperature of the system is function of the kinetic energy which in turn is determined by the velocities of the particles in the system. Thus one of the ways to maintain a constant temperature is by controlling or scaling the velocities of the particles. This process is known as the 'velocity rescaling method'.

If $T_{initial}$ be the starting temperature, and $T_{desired}$ be the temperature desired in the next step, then the scaling factor λ can be obtained from:

$$\Delta T = \frac{1}{2} \sum_{i=1}^N \frac{2}{3} \frac{m_i(\lambda v_i)^2}{N k_B} - \frac{1}{2} \sum_{i=1}^N \frac{2}{3} \frac{m_i(v_i)^2}{N k_B} = (\lambda^2 - 1) T_{initial} \quad (2.14)$$

Therefore,

$$\lambda = \sqrt{\frac{T_{desired}}{T_{initial}}} \quad (2.15)$$

If the desired and the initial temperatures are the same, then the value of λ will be unity. This is the simplest process to control temperature. Other thermostats include the Berendsen thermostat[89], the Andersen thermostat[90] and the Nosé-Hoover thermostat[91][92][93]. Out of these the Nosé-Hoover thermostat is the most popular and also the most accurate and efficient. It adds an extra degree of freedom with an associated effective mass in the lagrangian for the heat bath.

- **Constant pressure simulations:** The method to control pressure is similar to that of controlling the temperature except that in this case the volume is rescaled. This involves rescaling the particle coordinates and the length of the simulation box by a factor μ where:

$$\mu = \left[1 - \frac{\delta t}{\tau_p} (P - P_0) \right]^{1/3} \quad (2.16)$$

where τ_p is the time constant of the exponential decay from the current pressure P to the desired pressure P_0

Based on these thermostats and barostats a number of thermodynamic ensembles have been defined in molecular dynamics. Our study involves the use of NVE, NVT and NPT ensembles using Nosé-Hoover thermostat and barostats wherever necessary.

Chapter 3

Methodology

3.1 Tools and programs

The Molecular Dynamics simulations were done using LAMMPS package[94]. The data analysis was done using Python and Visual Molecular Dynamics (VMD)[95]. A brief introduction to LAMMPS and the calculation methods used in our study are presented below.

3.1.1 For Molecular Dynamics Simulations

LAMMPS is an ideal choice for performing MD simulations. It is an open-source software having good versatility, parallel performance having a very active user community. A typical LAMMPS input file requires the following fields:

- **Units:** It specifies the unit in which all the input and out parameters will be expressed. Some of the unit styles include lj (after Leonard-Jones interaction), metal, real, si, etc. The lj unit style specifies the energy in units of ϵ and the distance in terms of σ provided in the lj interactions while the other styles specifies all the quantities in terms of units we are familiar with.
- **atom style:** The atom_style command is used to specify the type of particles present in the system. It can be atoms only, atoms with bonds and angles or molecules having bonds, angles and dihedrals.
- **Defining the simulation box and the system:** This step is one of the most important ones. It specifies the geometry of the system to be simulated. For crystal systems the arrangement of the crystal lattice and the dimensions of the simulation box can be directly specified. For complex systems, this can be imported from a data file which contains all the information about the geometry of the molecules.
- **Groups:** Some of the particles (atoms or molecules) can be grouped together. For example, in a system containig a solution the solute and the solvent molecules can be seperated into two groups. These groups can be selectively operated differently in the simulation.
- **Attributes:** The next step requires specifying the different attributes for the particles like mass, initial velocities of all the atoms, etc.
- **Pair-Style:** The pair_style command in LAMMPS is used to specify the nature of interacting forces between each of the atoms. Lj/cut (Leonard-Jones potential with a cut-off), comb, FENE are some of the many available choices.
- **Fixes:** Fixes are required to simulate the system. The conditions of the simulation are defined by these fixes. For example, fix NVE will simulate the system using integrators in NVE ensemble. Fixes can be used to fix different attributes of the system as well. There are a variety of fixes used in this project, out of which, the fix bond/create is used to simulate the bond formation during the ion-irradiation process.
- **Computes:** LAMMPS provides options for calculation for many local (for each of the atoms individually) and global (for the system as a whole) properties.

- **Output:** All the outputs of LAMMPS can either be printed on the screen using the 'thermo' command or can be saved into a file using the 'dump' command.
- **Run:** The run command specifies the number of steps for the simulation to run.

3.1.2 For Data Analysis

Data analysis is also an important part of the study. The output data obtained from LAMMPS was analyzed using Python and VMD using the following developed tools:

- **Radial Distribution Function (RDF):** The radial distribution function or the pair correlation function $g(r)$ is a quantitative measure of the variation of density as a function of distance. The RDF function was implemented using python. The first step of the algorithm involves defining the density of the system:

$$\rho = N/V \quad (3.1)$$

Where N is the number of particles in the simulation box and V is the volume of the simulation box.

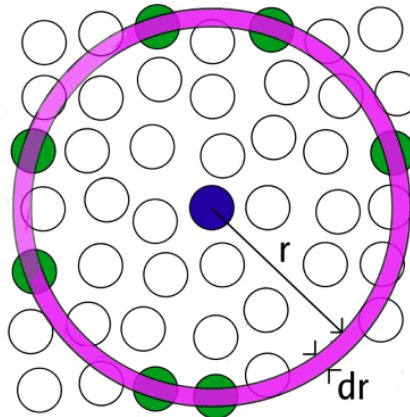


Figure 3.1: Calculation of the RDF. The particles highlighted in green lies within the strip between r to $r + dr$

Next the bin size (dr) and the maximum distance upto which the RDF is to be calculated (R_{max}) is chosen, the minimum (R_{min}) being 0. Smaller the bin size, greater will be the accuracy of the curve. For our calculations we have chosen a bin size of 0.05 units. The total span ($R_{max} - R_{min}$) is divided into $((R_{max} - R_{min})/dr)$ equal bins with different radii. The reference particle is placed at the origin. The number of particles n lying between radius r to $r + dr$ is assigned to the bin of radius r . This n is then averaged over all the particles and normalized by dividing it by the volume of the shell $dV = 4\pi(r + dr)^2 - 4\pi r^2$ and the total number of particles N ; and plotted as a function of r . If the simulation is performed using periodic boundary conditions, then they have to be implemented in the program as well as we have done for the simulation of Copper lattice and in that case R_{max} cannot exceed half the length of the box. RDF provides us a lot of valuable information like the probability of finding a particle at a given distance from any particle and the location of the neighboring particles in the simulation box which in turn provides the type of unit cell of the system. For example if an FCC structure changes to BCC after simulation, we can detect it using RDF.

- **Center of Mass Distance (COM) and Root-Mean Square Deviation (RMSD):** The RMSD calculation is done primarily in biological systems to inspect the stability of a molecule during the simulation. This is done by comparing the structure of the molecule for every step and plotting it as a function of time. The RMSD is calculated using a program developed using Python using the formula:

$$RMSD(\mathbf{r}_i, \mathbf{r}'_i) = \sqrt{\frac{1}{n} \sum_{i=1}^n ((r_{ix} - r'_{ix})^2 + (r_{iy} - r'_{iy})^2 + (r_{iz} - r'_{iz})^2)} \quad (3.2)$$

Here \mathbf{r}_i represents the position of the i^{th} particle at a particular timestep and \mathbf{r}'_i represents its position at some other timestep. n represents the number of particles in the system. The RMSD of a stable structure will typically initially increase with timesteps and then settle (with small fluctuations) at a small value as time progresses. On the other hand, RMSD of an unstable molecule will not saturate or saturate at a very high value which indicates change in the structure.

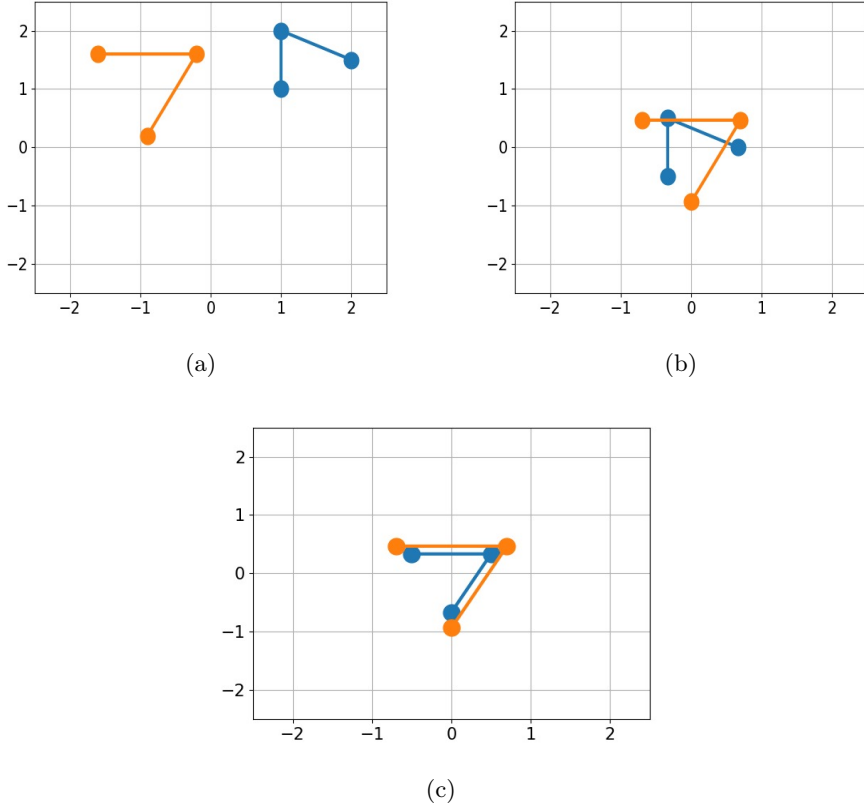


Figure 3.2: Schematic representation of the operations performed in RMSD calculation. The figure shows configurations of a simple molecule in 2D (a) initially at two different timesteps (b) when the COMs of the molecules are made to coincide. (c) when a rotation operation is performed to superpose one structure on another. After this step the RMSD can be calculated.

During simulation the molecule is free to move along all three axes as well as rotate about any axis. Before RMSD calculation we need to orient the molecule in such a way that these translational and rotational changes are nullified and only other structural changes remain which is an extremely difficult process. First, we need to find the center of mass coordinates of both the configurations as:

$$\mathbf{R}_{\text{cm}} = \frac{1}{M} \sum_{i=1}^N m_i \mathbf{r}_i \quad (3.3)$$

and set the COM of both of them to 0. Now the configuration at a later timestep is rotated using the Quaternion rotation algorithm. This is followed by the calculation of RMSD using equation 3.3.

- **Solvent Accessible Surface Area (SASA):** As the name suggests, SASA is defined as the surface area of a structure that is available to a solvent molecule. The surface area depends on the radius of the solvent molecule (probe radius) and in general chosen as 1.4 Å which is the radius of the water molecule. The SASA was calculated using a script in VMD which is based on a simple point-based random sampling method called the Shrake-Rupley algorithm.

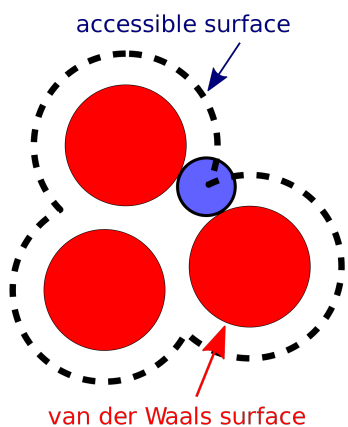


Figure 3.3: Measurent of solvent accessible surface area of the three atoms (shown in red) using a probe with a smaller radius (shown in blue)

In this method, each atom is represented by a number of points (here 500) randomly spread on the surface of it. If these points coincide for any two or more atoms, they are removed from the system. The remaining representative points forms the surface for the probe to measure. The probe used is a sphere with desired radius (generally the radius of the solvent molecule) and the surface area is measured by the number of points of the surface that coincide with the probe sphere.

Chapter 4

Some Basic Simulations to Get Started

Before proceeding to the actual problem I simulated a copper lattice and two proteins to get familiar with MD. This also provided with the opportunity to test the programs that we have developed for our study.

4.1 Simulation of Copper lattice

A three dimensional FCC copper lattice was simulated in the NVE ensemble for 10000 steps with each timestep = 0.02 picoseconds. The unit style 'metal' was used for the simulation. The first step included the model building. The mass of each atom was defined to be 63.54 grams/mole and the lattice constant (a) was set to 3.615 Å. The simulation box was chosen to be a cube with dimensions $4a \times 4a \times 4a$ with a being the lattice constant.

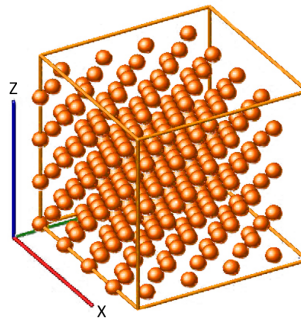


Figure 4.1: A snapshot from the Copper lattice simulation in NVE

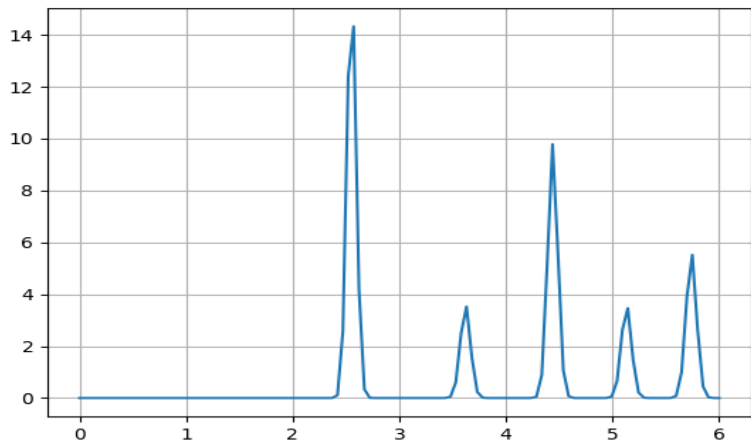
The force field used was comb which can be expressed as:

$$E_{total} = \sum_i [E_i^{self}(q_i) + \sum_{j>i} [E_{ij}^{short}(r_{ij}, q_i, q_j) + E_{ij}^{Coul}(r_{ij}, q_i, q_j)] + E^{polar}(q_i, r_{ij}) + E^{vdW}(r_{ij} + E^{barr}(q_i) + E^{corr}(r_{ij}, \theta_{jik})]] \quad (4.1)$$

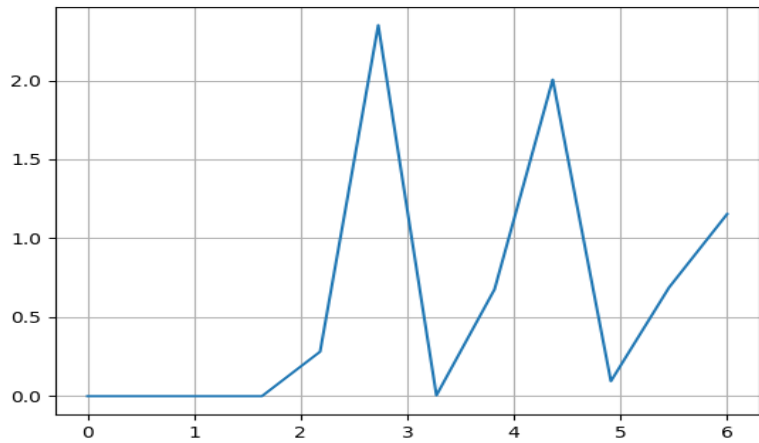
Where, E_i^{self} stands for the self energy of the i^{th} atom, E_{ij}^{short} for the bond-order potential between the i^{th} and the j^{th} atom, E^{Coul} for the Coulombic interactions between the charged particles, E^{polar} , E^{vdW} , E^{barr} and E^{corr} represents the polarization energy for organic systems, van der Waal's interaction energy, charge barrier function and the angular correction terms respectively.

We can check the structure of the lattice after the simulation using the radial distribution function.

- **RDF results** The final structure was analysed using the RDF program developed using two different bin sizes of 0.5 and 0.05 Å. The graphs in figure 4.2 obtained shows the requirement



(a)



(b)

Figure 4.2: Radial distribution function calculated after simulation of the Copper lattice (a)using a bin size of 0.5 \AA .(b)using a bin size of 0.05 \AA . The peaks indicate the location of the neighboring atoms which matches that of a FCC lattice.

of choosing a small bin size for accuracy. Henceforth, a bin size of 0.05 was used for future calculations. The lattice constant was chosen to be 3.615 Å. The peaks in figure was obtained at $2.56\text{ \AA} (= a/\sqrt{2})$, $3.62\text{ \AA} (= a)$, $4.43\text{ \AA} (= \sqrt{3}a/\sqrt{2})$ and so on which shows that the structure is still an FCC. Thus RDF can be used to determine the lattice structure or know about the location of the nearby neighbors. The latter property has been used at a latter stage to analyse the structure of the nanowires.

4.2 Simulation of Biomolecules

The program developed to calculate RMSD was used to analyze the stability of two simple protein structures, Plasmodium Falciparum SERA Protein (pdb id: 2muj)[96] and human Erythrocytic Ubiquitin (pdb id: 1ubq)[97] in water. The pdb files for the two proteins were obtained from the RCSB protein database[98].

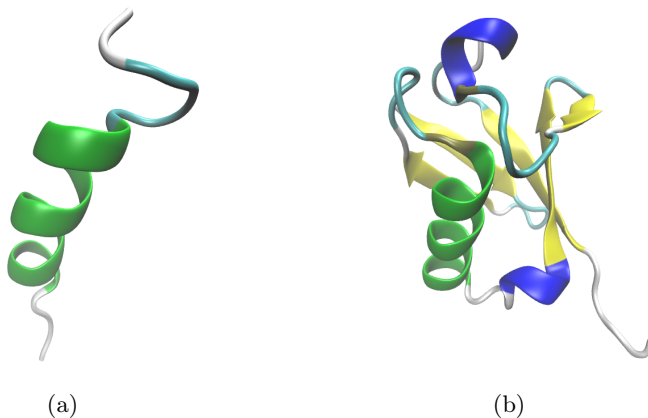
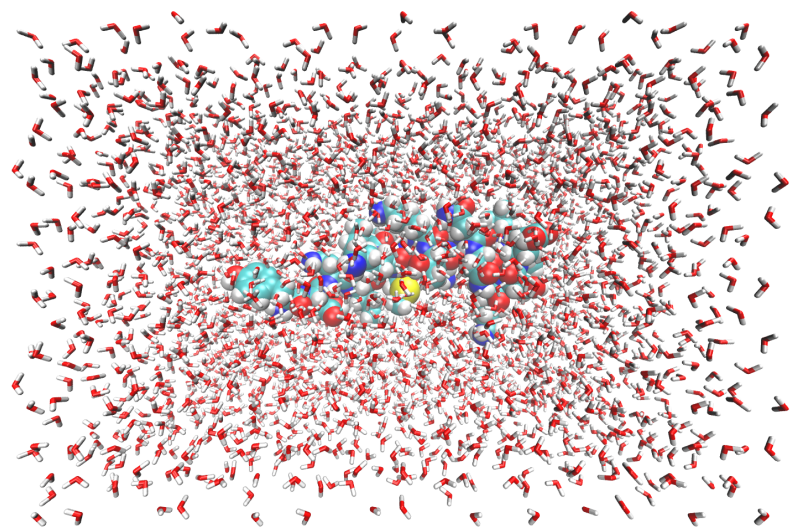


Figure 4.3: Sctuctures of (a) Plasmodium Falciparum SERA Protein (pdb id: 2muj) and (b) Human Erythrocytic Ubiquitin (pdb id: 1ubq) proteins, obtainend from RCSB protein database[98], rendered using VMD.

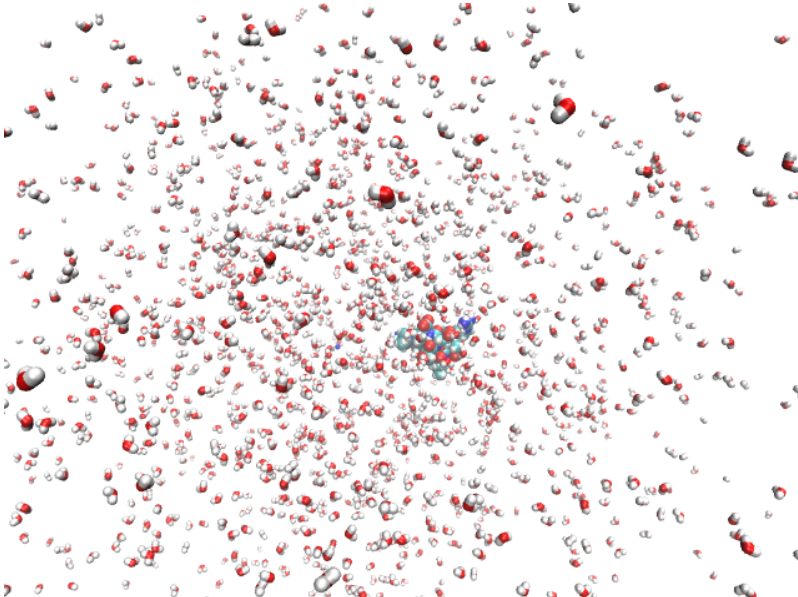
Next, they were solvated with water molecules to mimic a protein solution using VMD. A schematic of the simulation box after the solvation process is presented in figure 9(a). The modified pdb file was then used to obtain a topology file using AmberTools[99]. The pdb file contains the coordinates of all the atoms of an experimentally determined (using NMR or X-ray spectoscopy) protein structure in the form of a crystal, whereas, the topology file (with the extension '.prm-top') contains information about the charge, mass and type of all the atoms in all the residues. Furthermore, it also contains information about the bonds, angles and the dihedrals in the system which are essential when considering interactions between the atoms. The next step was to create a LAMMPS data file using the pdb and topology files and a LAMMPS input file to simulate the system. The CHARMM force-field was used for the neutral atoms and the coulomb force-field for for the charged ones. Both the systems were subjected to 500 steps of minimization to reduce the risk of crashing during the heating process and then heated in the NVE ensemble from 0 K to 300 K or room temperature using a Langevin thermostat. This was followed by equilibration under the NPT ensemble for about 5 millions steps with a stepsize of 1.0 fs. The final step in the simulation process was the production process of 2 million steps which was also carried out in the NPT ensemble with the same timestep. The last 150000 steps (i.e, 300 frames) of the production was used for the stability analysis.

Stability analysis

The stability of both the proteins were analysed by comparing their change in conformations as a function of the number of frames/timesteps. The initial and the final structures of both the proteins before and after the final 300 frames (0.15ns) of the simulation are presented in figure 10. Here the water molecules are removed for the ease of visualization. The snapshots indicate



(a)



(b)

Figure 4.4: Snapshots from the simulation of 2muj protein in water (a) before the simulation (b) during the production run (with unwrapped boundaries), rendered using VMD.

negligible changes in the protein conformation as we would expect and this was further confirmed by the RMSD calculations

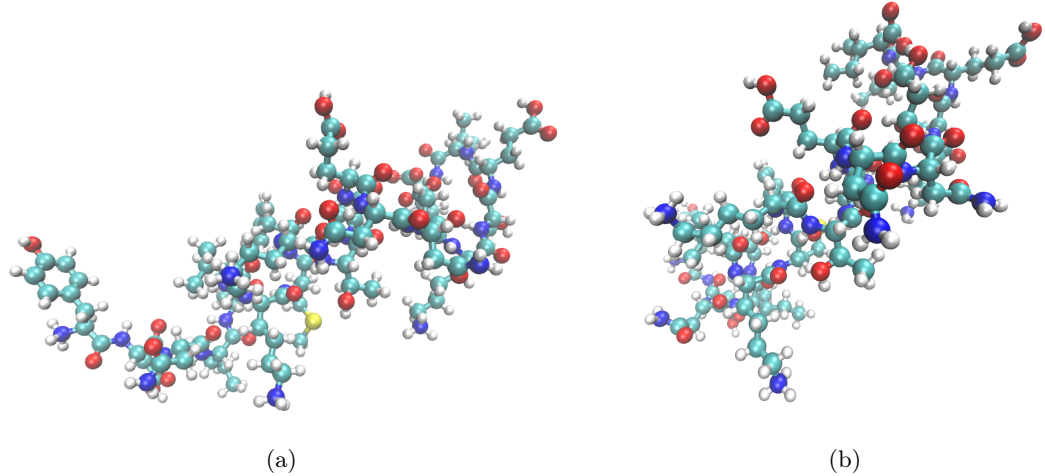


Figure 4.5: Snapshots of only the protein from the simulation of 2muj in water (a) before the final 0.15ns (b) after the final 0.15ns of the production, rendered using VMD.

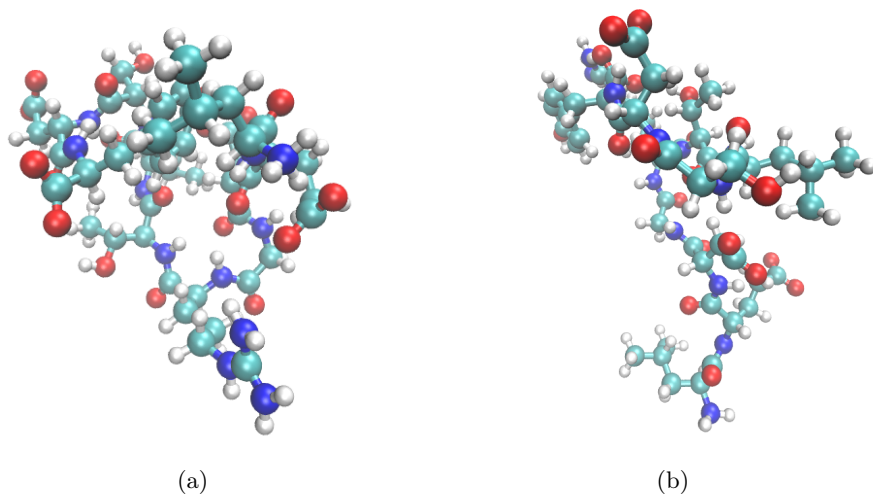
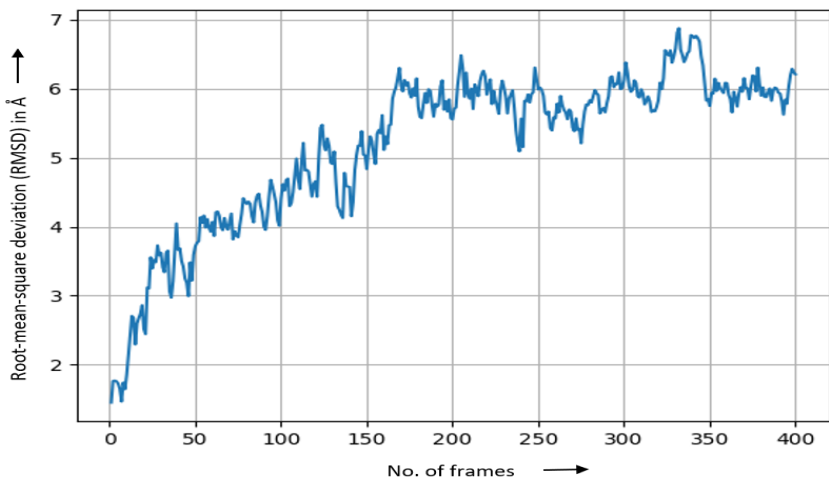
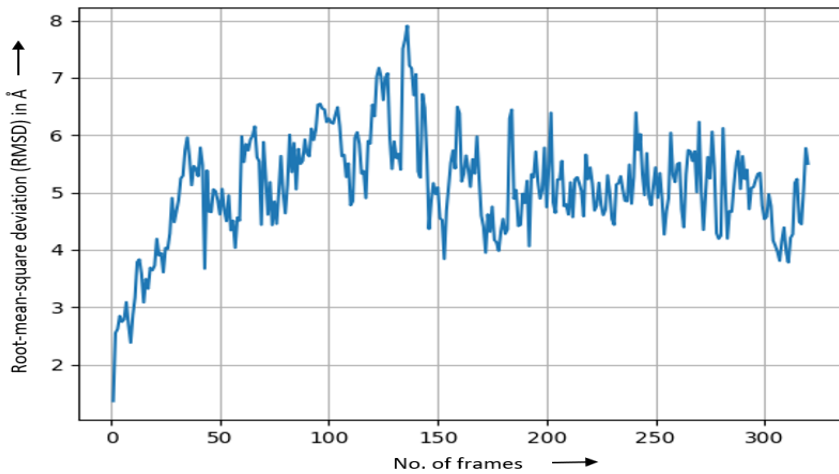


Figure 4.6: Snapshots from the simulation of 1ubq protein in water (a) before the final 0.15 ns (b) after the final 0.15 ns of the production run, rendered using VMD.

The first of the final 300 frames was considered as the reference frame for both the proteins and root-mean-square deviation (RMSD) was calculated for all the remaining frames with respect to that one. The RMSD vs the number of frames graphs agrees with the snapshots and proves the stability of the proteins throughout the simulation.



(a)



(b)

Figure 4.7: Plots of RMSD vs number of frames (1 frame = 500 fs) for (a) 2muj (b) 1ubq, for 0.15 ns frames of production.

The RMSD increases initial in both the simulations and after about 150 frames (0.075 ns) settles at a value of about 5 Å for 1ubq and 6 Å for the 2muj which are acceptable for a stable structure.

Chapter 5

Simulation and Results

The study of the effect of ion beam irradiation was studied using coarse-grained Molecular Dynamics (CGMD) simulations. For this purpose, two different lengths of nanowires were used: (a) One with 100 beads or pseudo-atoms per chain and (b) another with 1000 pseudo-atoms per chain. The entire simulation process in both cases can be divided into four sections: (a) Modelling the nanowires (b) simulating the ion-beam irradiation on the nanowires (c) measurement of the solvent accessible surface area (SASA), Root-mean-squared distance (RMSD) and Radial Distribution Function (RDF), and (d) Results and Analysis.

5.1 Simulating Nanowires with a Hundred Pseudo-atoms per Chain

We start with the simulation of the shorter nanowires. The entire study can be divided into the following sections.

5.1.1 Modelling the nanowires

The first step of the simulation was to model for the nanowires. A single nanowire is modelled by a chain of 100 beads where the radius of the bead equals the radius of the nanowire. Each bead would typically contain about 50 to 100 atoms. Instead of creating an interwind network of nanowires, we started with a 10×10 matrix of wires as shown in figure 13. The coordinates of each of the bead was provided in a data file to be read during the simulation.

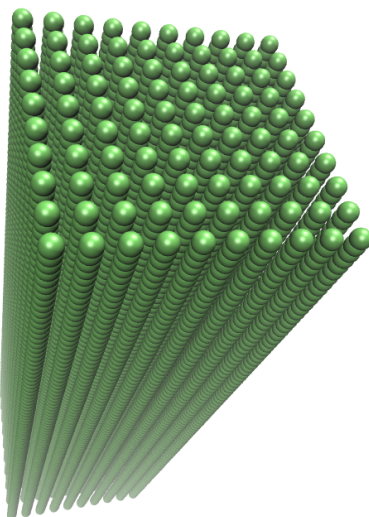


Figure 5.1: Nanowire matrix at the start of the simulation

The unit style ‘lj’ was used throughout the simulation i.e., all the quantities were specified in terms of ‘ ϵ ’ (having dimensions of energy) and ‘ σ ’(having dimensions of length). A combination of two Leonard-jones potentials of different strengths and ranges was chosen as the force field - one with potential depth of 1.0ϵ and extending upto 1.12σ to prevent the wires from coming too close to each other and another with depth 0.001ϵ and a range of 2.5σ which provides a very weak attractive force to prevent the wires from escaping the simulation at a rate faster than that of the simulation. Other possible force fields were also considered but they either resulted in an unstable simulation or produced other unfavourable situations.

Before beginning the simulation 500 steps of energy minimizations were performed. Energy minimization involves minimizing the energy by changing the coordinates of the atoms in an iterative way. This ensures that the stability of the system before the start of the simulation.

5.1.2 simulation process

Next, the system was heated from temperature 0 to 1.0 unit in the NVE ensemble using a Langevin thermostat. This was followed by a million steps of simulation in the NVT ensemble at the same temperature and a further 5 million steps of simulation in the NPT ensemble using a Langevin barostat to fix the pressure at 0.01 unit. The size of the time step was 0.001 for all the simulations and the values of temperature and pressure used in the simulation are standard for this type of simulation.

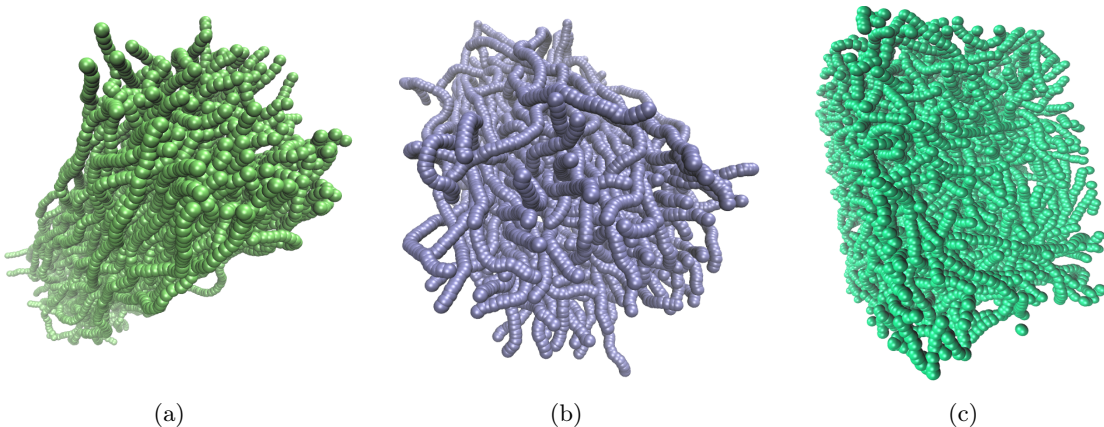


Figure 5.2: Configuration of the nanowires after simulations in the (a) NVE ensemble, (b) NVT ensemble, and (c) NPT ensemble, rendered using VMD.

These simulations were performed in order to equilibrate the system. As can be seen from figure 14, the heating process does not significantly change the nanowire network. The nanowires begins to bend and interwind around each other in the NVT simulations and the NPT simulation compresses the system until an equilibrium is reached between the pressure of the system and the external pressure. NPT simulations were initially performed at a pressure of 1.0 unit. However, it proved to be too high for the sample and it compressed a lot more than it should. Hence, the external pressure was reduced to 0.01 unit.

5.1.3 Simulation of ion-beam radiation

The effects of ion-beam radiation as reported by many was incorporated into the simulation by allowing creation of a special type of bond using the ‘bond_create’ command in LAMMPS. After the initial equilibration, the system was further simulated for 100,000 steps followed by 600,000 steps of simulation in which bonds were allowed to form every 10,000th step. This was followed by a production time of 500,000 steps. All the simulations were done in the NPT ensemble. The ‘bond_create’ command was used with the parameters $r_{min} = 1.1\sigma$ and probability of 1% which means that new bonds can be formed only when two atoms are seperated by a distance less than or equal to r_{min} with a probability of 1%.

An identical system was created by following the same steps with the 600,000 steps of bond formation replaced by simple NPT simulations of the equal number of steps. This was done to compare the systems - the unmodified nanowires and the ion irradiated ones directly.

5.1.4 Comparison and Results:

As mentioned above, the SASA depends on the radius of the probe. As an example, we have provided the configurations of the surface accessible to two different solvent molecules of radii 0.2 and 0.8 in figure 15. The radius of the water molecule in real units is about 1.4 Å. So we can expect the water droplets to have radius of about 0.8 in reduced units which is used as the probe radius.

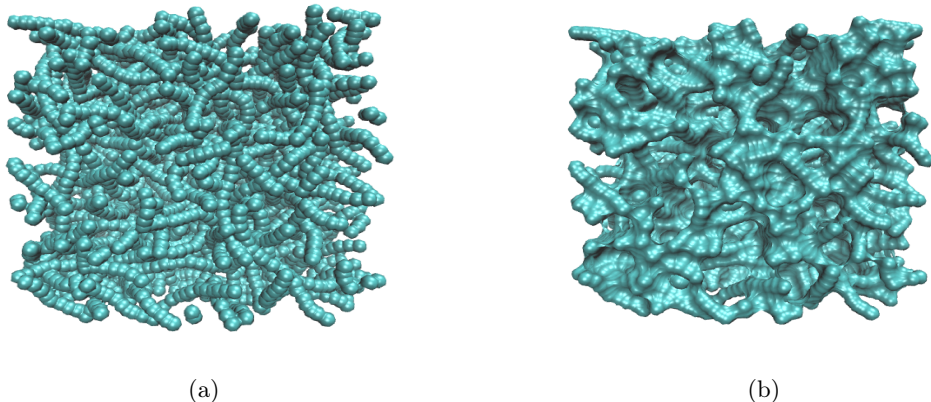
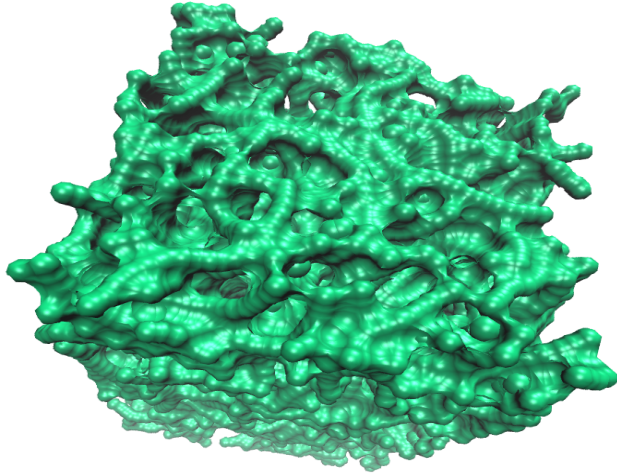
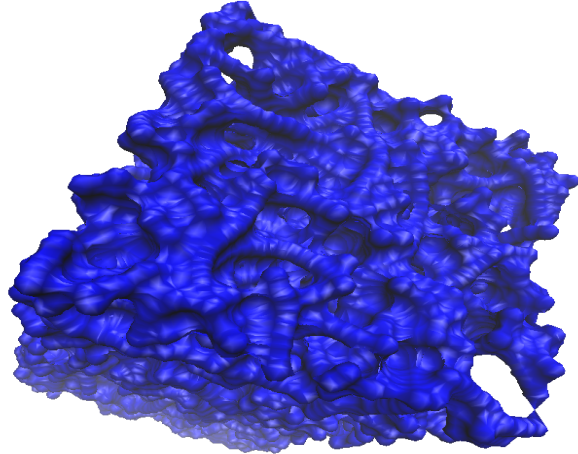


Figure 5.3: Configuration of the nanowires after simulations in the (a) NVE ensemble, (b) NVT ensemble, and (c) NPT ensemble, rendered using VMD.

In our simulation, 147 bonds were formed between the 100 nanowires. Simulations with higher bond formation probabilities were also performed but a very large number of bonds actually decreased the surface area instead of increasing it.



(a)



(b)

Figure 5.4: Configurations of the surface when (a) excess bonds are allowed to form, (b) excess bonds are not allowed to form, rendered using vmd. If looked closely, configuration (a) looks more porous than configuration (b)

If we closely look at figure 16(a) and 16(b) it appears that figure 16(a) is more porous than (b). So the snapshots agree with our result. The measured SASA was not completely fixed but was slowly varying with the simulation about a mean value, which is expected. As a result, we have calculated the SASA over a range of values. The average increment in the surface area with probe radius of 0.8 unit was found to be 4.718% on an average with the maximum being 6.7% . RDF analysis was also conducted in the two cases and the plots are presented in figure 18. It can be seen that the newly created bonds after equilibration have forced some of the atoms to shift further from their equilibrium position causing to form two distinct peaks instead of the one which is formed in case there is no ion irradiation.

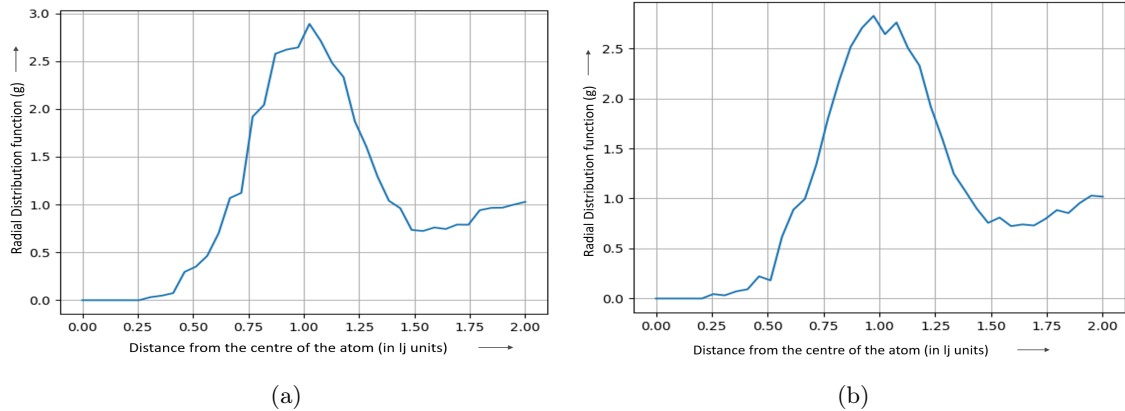


Figure 5.5: The radial distribution function plotted for (a) the unmodified system (b) the irradiated system.

5.1.5 Variation with temperature

The variation of the SASA was also studied as a function of temperature. The equilibrated systems (both modified and unmodified) were heated to a temperature of 2.0 unit in one case and cooled down to 0.8 unit in another case to study their behaviour. It was found that the unmodified system was far more sensitive to temperature than the modified one. In the heating process both the volume and SASA of the modified system was found to be much less than the unmodified one. However, during the cooling process both the volume and SASA increased with the average SASA being about 15% more than the unmodified nanowires.

5.2 Simulating Nanowires with a Thousand Pseudo-Atoms per chains

Now, we move on to the longer nanowires. This reduces the extent of coarse-graining and consequently greatly increases the computational time. However it increases the molecular detail and represents a much more realistic system. The entire study has been divided into the following sections.

5.2.1 Coarse-Grain Modelling the Nanowires

The coarse-grained model of the nanowire-array was built by creating a ‘xyz’ type file using Python. A 10×10 matrix of chains were constructed with each chain having 1000 beads as shown in figure 5.6. The chains were treated as molecules with each of them being assigned an unique molecule id and the beads were treated as atoms with unique atom ids. The beads belonging to the same chain were separated by 1.0 unit of space and the chains were separated from each other by 50 unit to construct a stable initial starting point.

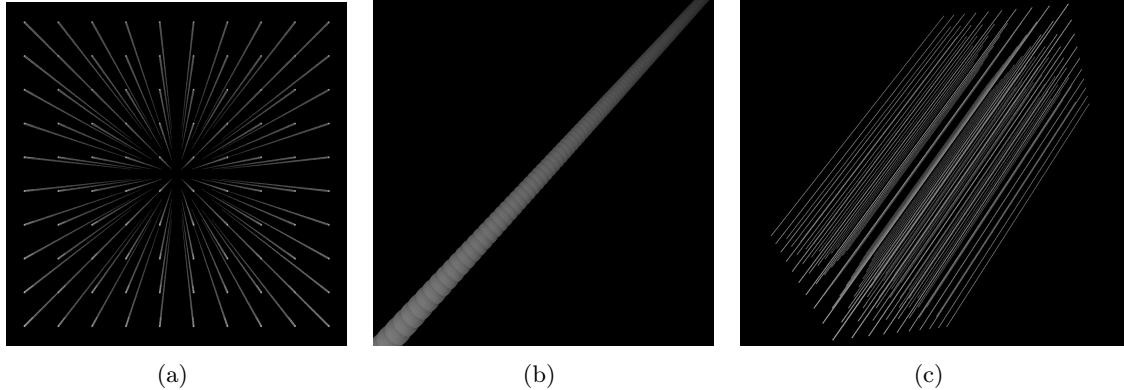


Figure 5.6: Model of the nanowire matrix: (a)front view (b)zoomed in view of a single chain. (c)side view of the nanowires

The next step was to convert the ‘xyz’ file into a lammps data file (a file which can be understood by lammps). This requires providing information about bonds, angles and the mass of the beads which was done using the TopoTools package in the Visual Molecular Dynamics (VMD) software. Initially, the radius and mass of the beads are set to 0.85 and 1.0 respectively in the Leonard-Jones (lj) units. All the beads are assigned the same atom type and a Python program was later used to differentiate the chains by allocating different molecule ids to them. The TopoTools package was used to create bonds between the beads of the same chain and the bond angles were set to 180° to get straight chains initially. There were a total of 100,000 beads/atoms, 99,900 bonds and 99,800 angles. The dimension of the nanowire matrix was evaluated to be 460 × 460 × 1000 cubic unit and the dimension of the simulation box was chosen to be 1000 × 1000 × 1500 cubic unit to allow extra space for the simulation. The interaction force between the atoms was very carefully chosen so that the chains would neither come very close to each other and nor be driven away violently by the strong but short-ranged repulsive force. This was done by choosing a hybrid pair style comprising of two lj interaction forces of different strength and range: (a) ‘lj/cut’ pair style with ϵ value of 1.0, σ value of 1.0, and a cutoff (r_c) of 1.12, and (b) ‘lj/smooth’ pair style with ϵ value of 0.004 and σ value of 1.0 with the inner cutoff (r_{in}) and outer cutoff(r_c) set to 1.12 and 2.5 units respectively. This model was then subjected to a variety of different simulation techniques using LAMMPS simulation software.

5.2.2 Simulating the Nanowires

The first step in the simulation was the energy minimization. This is done by iteratively changing the coordinates of the atoms in order to drag the system to a local potential minimum so that the system is at a relatively stable state when the simulation starts. The function that is minimized to obtain the optimum atom coordinates is known as the objective function and is given as:

$$E(r_1, r_2, \dots, r_N) = \sum_{i,j} E_{pair}(r_i, r_j) + \sum_{i,j} E_{bond}(r_i, r_j) + \sum_{ijk} E_{angle}(r_i, r_j, r_k) + \sum_{ijkl} E_{dihedral}(r_i, r_j, r_k, r_l) + \sum_{ijkl} E_{improper}(r_i, r_j, r_k, r_l) + \sum_i E_{fix}(r_i) \quad (5.1)$$

In our case, only E_{pair} , E_{bond} and E_{angle} terms are non zero, since there are no dihedrals, impropers or fixes present at this stage. The minimization was carried on for 500 steps with the minimization style (‘min_style’ command) known as the ‘steepest descend (sd) algorithm’.

The minimization was followed by constant number (N), volume (V), and energy (E) simulation, otherwise known as NVE or microcanonical simulations, in presence of a langevin thermostat. The initial temperature of 0.0 lj unit was slowly increased to 1.5 unit through a series of steps

using the said thermostat. Throughout the simulation, the chains were treated as rigid bodies and any type of bending or stretching was prohibited. The rigid wires, however, were allowed to move and rotate. This allowed to replicate the pristine and rigid nanowires shown in figure 1.3.

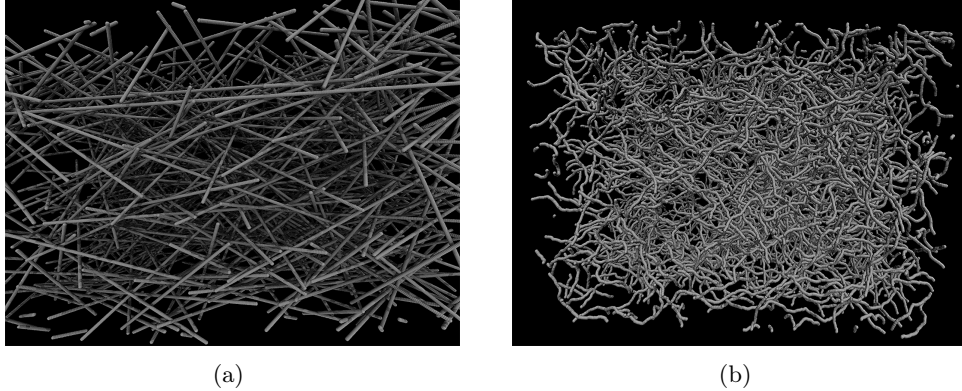


Figure 5.7: Snapshot of the nanowires (a) during the NVT simulation of the rigid nanowires (c) during normal NVT simulations without applying the rigid constraint

The next step was to remove the rigid constraint from the wires and continue with the simulations. This introduced minor bends in the nanowires as shown in figure 5.7(b). The next step was to apply a small amount of pressure to simulate the laboratory conditions. For this purpose, a barostat was employed. The fix ‘press/berendsen’ was used as the choice of barostat along with the Langevin thermostat which was used to maintain a constant temperature of 1.5 unit. The sudden application of high pressure could force the beads to come within the cut off region which would cause the beads to experience a very strong force suddenly, kicking them away from the simulation box. To avoid this, a low pressure was exerted in the beginning which was then increased to the desired value at a later stage of the simulation. This combination of the Berendsen barostat and the Langevin thermostat has been preferred over the conventional fix ‘npt’ in other papers involving cross-linking polymers as well[100]. This was done to achieve a greater deal of stability of the system. The stability of the system was measured using the RMSD calculations for each atom as a function of the number of frames.

The system was compressed to three different pressures of 0.1, 0.01 and 0.001 unit keeping the temperature fixed at 1.5 units and bond formation was simulated in each of the systems. The more compressed systems took more time to equilibrate than the less compressed ones. However, the system having the most potential to show significant changes in the surface area is the most compressed one.

5.2.3 Simulating the Ion-Beam Irradiation Process

The ion-beam irradiation process was indirectly simulated by creating special type of bonds as encountered in various studies[49][71][72][73][74]. The bonds were created by using the fix ‘create/bond’ with different probabilities. Instead of using any temperature dependent criteria for creating the bonds, the distance between the atoms were used as the deciding factor for the bond formation. A cut off value of 1.2 unit was chosen for the fix with the different probabilities deciding the concentration of the irradiation. The bond formation process led to the formation of the ‘X’ type bonds between the nanowires that we have seen in the carbon nanofibres. This type of bonds was absent in the previous study where nanowires with 100 beads were subjected to the same process.

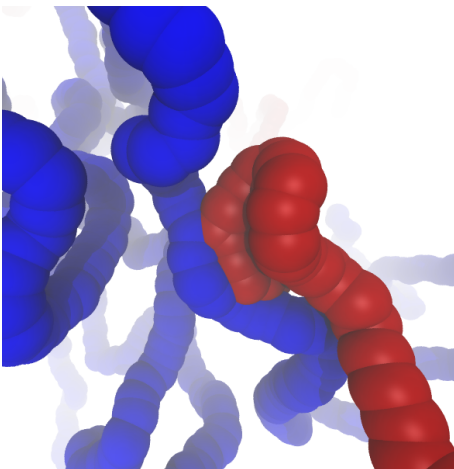


Figure 5.8: A snapshot captured after the process of bond formation showing multiple bonds at the same location between two nanowires colored in red and blue. The snapshot is rendered using VMD.

A total of around 2,000 bonds were created for the 100,000 atoms when a probability of 0.002 was used for the system equilibrated at 0.1 unit of pressure. However, for the less compressed systems, the same number of bonds can be formed with a higher value of probability. This can be easily explained by the fact that closer the atoms are to each other, more will be the number of bonds formed. The process of bond formation was divided into a number of steps and Sufficient time was provided between each step to stabilize the system before the next step of bonds are formed.

The formation of bonds restricts the independent movements of the nanowires and also leads to the development of an interconnected network or mesh which has proved to serve as a better alternative to unmodified nanowires. To understand the effect of the formation of such an interconnected network, the exact steps were repeated without the bond formation part, i.e, the unmodified nanowires were subjected to the same conditions of temperature and pressure for the same amount of time without exposing them to bond formation. The two structures were then compared to determine the effect on the surface areas. Both the Radial Distribution Function and the Solvent Accessible Surface Area calculations were carried out for the detailed analysis of the simulated structures. The details of the calculations are presented in the next section.

5.2.4 Analysis and Results

Stability analysis was done for the irradiated system by calculating the RMSD of the system and plotting it as a function of the number of frames in order to make sure that the system has equilibrated. The equilibration process was much more lengthy compared to that of the shorter nanowires, which is expected. The plot is presented in figure 5.9. Both the modified and the unmodified structures were directly compared to determine the effects of the irradiation. The average Solvent Accessible surface Area (SASA) was measured in both the cases using a probe radius of 0.7 units. The results indicated a minor decrease of 1.58% of the SASA upon irradiation. This is in contradiction to the study done on the shorter nanowires where the irradiation process increased the surface area. The results were further confirmed by RDF analysis of both the modified and the unmodified nanowires. The RDF plots are presented in figure 5.10. The irradiated system has higher peaks before $r = 1.05$ (indicated by the blue line in the graphs) which causes a small decrease in the SASA. A snapshot of the system after the irradiation process is completed is presented in figure 5.11

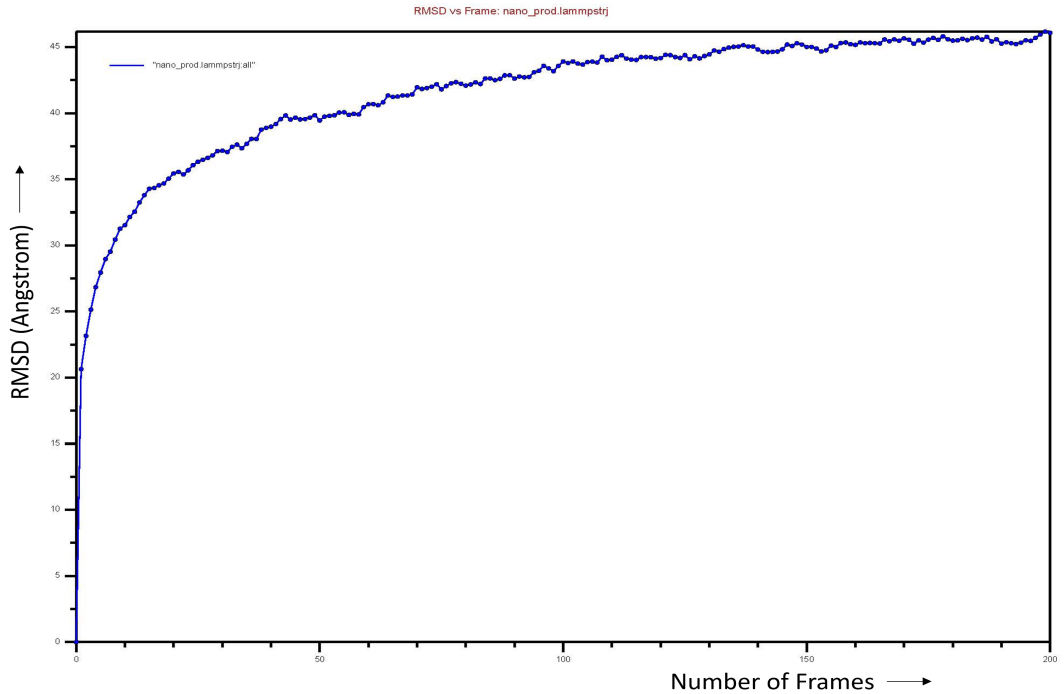


Figure 5.9: The Root-Mean-Squared Deviation (RMSD) of the irradiated nanowires plotted as a function of time/number of frames. (1 frame = 100 time units)

Similar analysis was also done by changing the new bond parameters (like bond length, bond strength, bond numbers) in order to understand their role in influencing the surface area. However, the results obtained were identical in each case except the fact that the surface area was found to decrease with increase in the number of bonds. With the decrease in pressure, the decrease in surface area of the irradiated system becomes more prominent and at very low pressures the decrement is fairly noticeable. All the simulations were carried out at a fixed temperature of 1.5 with a timestep of 0.01 unit.

5.3 Conclusion

The highly non-equilibrium process of ion-beam irradiation can alter both the chemical and structural properties of the sample. These changes can often give rise to enhanced functionality of the irradiated material. Our study focuses on the effects introduced in the accessible surface area as a result of the modification. We chose two different lengths of nanowires containing different number of ‘pseudo-atoms’ per chain for this study. The one containing about hundred pseudo-atoms per chain shows a moderate increase of surface area (around 7%) upon irradiation. However, the system with the longer nanowires shows a slight decrease (around 1.58%) in the surface area, under similar conditions of temperature and pressure. The system with the longer nanowires can better represent the conventional nanowires due to the fact that it preserves the molecular details better than the shorter nanowire system. That being said, the results indicate the presence of an optimum length, depending on the nature of the nanowires, for which the irradiation process can enhance the conductivity and further increase the effectiveness of the nanowires as electrode materials. Further studies can reveal this optimum length for different nanowire systems. If the surface area can be increased by the process of irradiation only, then it can be effective for all types of nanowires irrespective of their chemical composition, which can help us in our search for better electrode materials for constructing high-performance batteries.

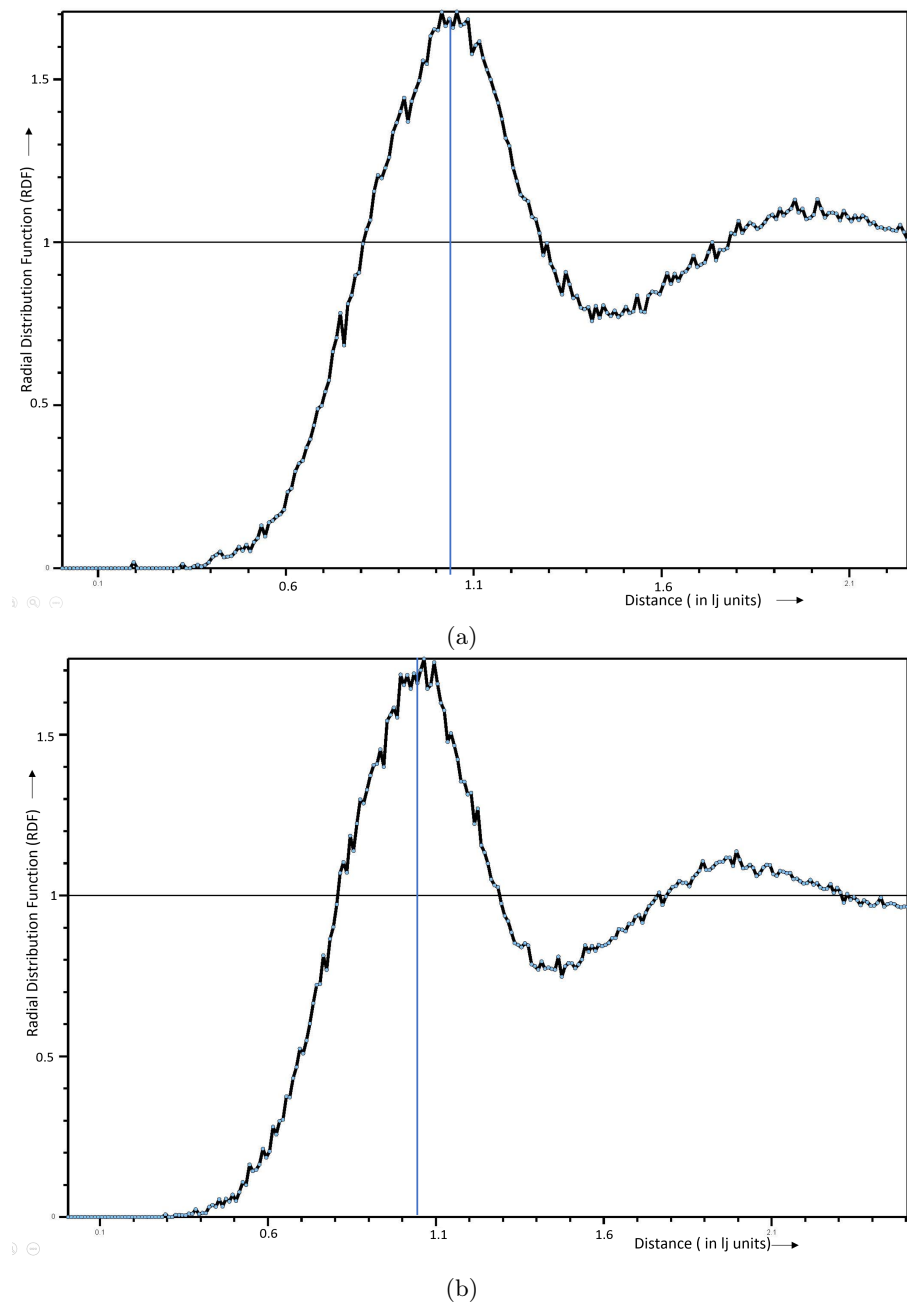


Figure 5.10: Radial Distribution Function (RDF) plotted as a function of the distance for (a) the system where bonds were allowed to form and (b) where bonds were not allowed.

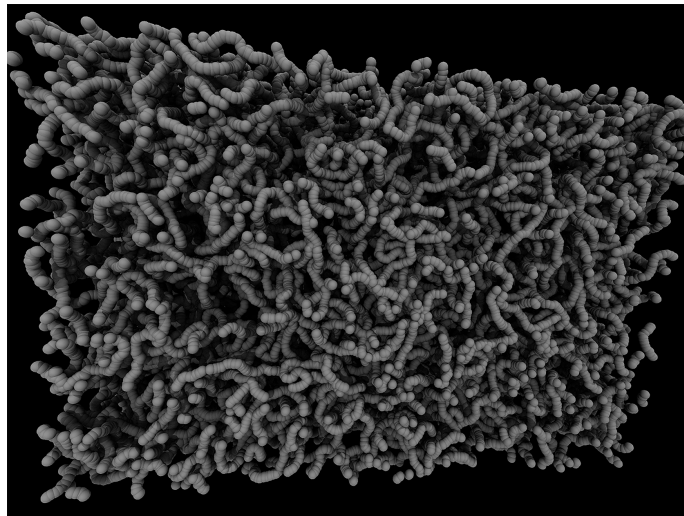


Figure 5.11: A snapshot captured during the equilibration process after the bond formation was completed.

List of Publications

- Co-authored a book chapter titled ‘Molecular Dynamics Simulations of 2D Materials’ along with Dr. Hemant Kumar in the book ‘Synthesis, Modelling and Characterization of 2D Materials and their Heterostructures’ to be published by Elsevier on 26th June 2020.
- Presently co-authoring another book chapter ‘Ion beam joining of similar and dissimilar materials’ along with Dr. Shyamal Chatterjee to be published by Elsevier.

Acknowledgement

I would like to thank my guide Dr. Shyamal Chatterjee for helping me understand the basics of ion-beam modification and for introducing me with the different experimental methods regarding the process; and also Dr. Hemant Kumar for teaching me Molecular Dynamics from scratch. Both have helped me extensively and have supported me throughout this project.

I would like to thank all the faculty of the physics department for their great support and for providing me the opportunity to work on such an interesting subject.

Finally, I would like to thank my family and my friends here at IIT Bhubaneswar for motivating me to do good work.

Bibliography

- [1] J. B. Goodenough and K.-S. Park, “The li-ion rechargeable battery: a perspective,” *Journal of the American Chemical Society*, vol. 135, no. 4, pp. 1167–1176, 2013.
- [2] J. B. Goodenough, “Electrochemical energy storage in a sustainable modern society,” *Energy & Environmental Science*, vol. 7, no. 1, pp. 14–18, 2014.
- [3] Y. Xia, P. Yang, Y. Sun, Y. Wu, B. Mayers, B. Gates, Y. Yin, F. Kim, and H. Yan, “One-dimensional nanostructures: synthesis, characterization, and applications,” *Advanced materials*, vol. 15, no. 5, pp. 353–389, 2003.
- [4] A. S. Arico, P. Bruce, B. Scrosati, J.-M. Tarascon, and W. Van Schalkwijk, “Nanostructured materials for advanced energy conversion and storage devices,” in *Materials for sustainable energy: a collection of peer-reviewed research and review articles from Nature Publishing Group*, pp. 148–159, World Scientific, 2011.
- [5] X. Chen, C. Li, M. Grätzel, R. Kostecki, and S. S. Mao, “Nanomaterials for renewable energy production and storage,” *Chemical Society Reviews*, vol. 41, no. 23, pp. 7909–7937, 2012.
- [6] C. K. Chan, H. Peng, G. Liu, K. McIlwrath, X. F. Zhang, R. A. Huggins, and Y. Cui, “High-performance lithium battery anodes using silicon nanowires,” *Nature nanotechnology*, vol. 3, no. 1, p. 31, 2008.
- [7] J. R. Szczech and S. Jin, “Nanostructured silicon for high capacity lithium battery anodes,” *Energy & Environmental Science*, vol. 4, no. 1, pp. 56–72, 2011.
- [8] P. Meduri, C. Pendyala, V. Kumar, G. U. Sumanasekera, and M. K. Sunkara, “Hybrid tin oxide nanowires as stable and high capacity anodes for li-ion batteries,” *Nano letters*, vol. 9, no. 2, pp. 612–616, 2009.
- [9] N. P. Dasgupta, J. Sun, C. Liu, S. Brittman, S. C. Andrews, J. Lim, H. Gao, R. Yan, and P. Yang, “25th anniversary article: semiconductor nanowires—synthesis, characterization, and applications,” *Advanced materials*, vol. 26, no. 14, pp. 2137–2184, 2014.
- [10] A. I. Hochbaum and P. Yang, “Semiconductor nanowires for energy conversion,” *Chemical reviews*, vol. 110, no. 1, pp. 527–546, 2010.
- [11] S. Yodyingyong, Q. Zhang, K. Park, C. S. Dandeneau, X. Zhou, D. Triampo, and G. Cao, “Zno nanoparticles and nanowire array hybrid photoanodes for dye-sensitized solar cells,” *Applied Physics Letters*, vol. 96, no. 7, p. 073115, 2010.
- [12] J. Jiang, Y. Li, J. Liu, and X. Huang, “Building one-dimensional oxide nanostructure arrays on conductive metal substrates for lithium-ion battery anodes,” *Nanoscale*, vol. 3, no. 1, pp. 45–58, 2011.
- [13] E. Hosono, T. Kudo, I. Honma, H. Matsuda, and H. Zhou, “Synthesis of single crystalline spinel limn₂o₄ nanowires for a lithium ion battery with high power density,” *Nano letters*, vol. 9, no. 3, pp. 1045–1051, 2009.
- [14] E. Hosono, T. Saito, J. Hoshino, M. Okubo, Y. Saito, D. Nishio-Hamane, T. Kudo, and H. Zhou, “High power na-ion rechargeable battery with single-crystalline na_{0.44}mno₂ nanowire electrode,” *Journal of Power Sources*, vol. 217, pp. 43–46, 2012.

- [15] L.-Q. Mai, F. Yang, Y.-L. Zhao, X. Xu, L. Xu, and Y.-Z. Luo, “Hierarchical $\text{mnmoo}_4/\text{comoo}_4$ heterostructured nanowires with enhanced supercapacitor performance,” *Nature communications*, vol. 2, p. 381, 2011.
- [16] W. Zhou, C. Cheng, J. Liu, Y. Y. Tay, J. Jiang, X. Jia, J. Zhang, H. Gong, H. H. Hng, T. Yu, *et al.*, “Epitaxial growth of branched $\alpha\text{-fe2o3}/\text{sno2}$ nano-heterostructures with improved lithium-ion battery performance,” *Advanced Functional Materials*, vol. 21, no. 13, pp. 2439–2445, 2011.
- [17] L.-F. Cui, Y. Yang, C.-M. Hsu, and Y. Cui, “Carbon- silicon core- shell nanowires as high capacity electrode for lithium ion batteries,” *Nano letters*, vol. 9, no. 9, pp. 3370–3374, 2009.
- [18] X. Xia, J. Tu, Y. Zhang, J. Chen, X. Wang, C. Gu, C. Guan, J. Luo, and H. J. Fan, “Porous hydroxide nanosheets on preformed nanowires by electrodeposition: branched nanoarrays for electrochemical energy storage,” *Chemistry of Materials*, vol. 24, no. 19, pp. 3793–3799, 2012.
- [19] J. Y. Huang, L. Zhong, C. M. Wang, J. P. Sullivan, W. Xu, L. Q. Zhang, S. X. Mao, N. S. Hudak, X. H. Liu, A. Subramanian, *et al.*, “In situ observation of the electrochemical lithiation of a single sno2 nanowire electrode,” *Science*, vol. 330, no. 6010, pp. 1515–1520, 2010.
- [20] X. H. Liu and J. Y. Huang, “In situ tem electrochemistry of anode materials in lithium ion batteries,” *Energy & Environmental Science*, vol. 4, no. 10, pp. 3844–3860, 2011.
- [21] A. Manthiram, Y. Fu, and Y.-S. Su, “Challenges and prospects of lithium–sulfur batteries,” *Accounts of chemical research*, vol. 46, no. 5, pp. 1125–1134, 2012.
- [22] S. Evers and L. F. Nazar, “New approaches for high energy density lithium–sulfur battery cathodes,” *Accounts of chemical research*, vol. 46, no. 5, pp. 1135–1143, 2012.
- [23] K.-Q. Peng, X. Wang, L. Li, Y. Hu, and S.-T. Lee, “Silicon nanowires for advanced energy conversion and storage,” *Nano Today*, vol. 8, no. 1, pp. 75–97, 2013.
- [24] C. Cheng and H. J. Fan, “Branched nanowires: synthesis and energy applications,” *Nano Today*, vol. 7, no. 4, pp. 327–343, 2012.
- [25] P. G. Bruce, S. A. Freunberger, L. J. Hardwick, and J.-M. Tarascon, “Li–o₂ and li–s batteries with high energy storage,” *Nature materials*, vol. 11, no. 1, pp. 19–29, 2012.
- [26] Y. Wang, T. Wang, P. Da, M. Xu, H. Wu, and G. Zheng, “Silicon nanowires for biosensing, energy storage, and conversion,” *Advanced materials*, vol. 25, no. 37, pp. 5177–5195, 2013.
- [27] J. Graetz, C. Ahn, R. Yazami, and B. Fultz, “Nanocrystalline and thin film germanium electrodes with high lithium capacity and high rate capabilities,” *Journal of The Electrochemical Society*, vol. 151, no. 5, pp. A698–A702, 2004.
- [28] H. Kim, Y. Son, C. Park, J. Cho, and H. C. Choi, “Catalyst-free direct growth of a single to a few layers of graphene on a germanium nanowire for the anode material of a lithium battery,” *Angewandte Chemie International Edition*, vol. 52, no. 23, pp. 5997–6001, 2013.
- [29] M. S. Whittingham, “Lithium batteries and cathode materials,” *Chemical reviews*, vol. 104, no. 10, pp. 4271–4302, 2004.
- [30] H.-W. Lee, P. Muralidharan, R. Ruffo, C. M. Mari, Y. Cui, and D. K. Kim, “Ultrathin spinel limn2o4 nanowires as high power cathode materials for li-ion batteries,” *Nano letters*, vol. 10, no. 10, pp. 3852–3856, 2010.
- [31] Y. Yang, C. Xie, R. Ruffo, H. Peng, D. K. Kim, and Y. Cui, “Single nanorod devices for battery diagnostics: A case study on limn2o4,” *Nano letters*, vol. 9, no. 12, pp. 4109–4114, 2009.
- [32] Y. Wang, Y. Wang, D. Jia, Z. Peng, Y. Xia, and G. Zheng, “All-nanowire based li-ion full cells using homologous mn2o3 and limn2o4 ,” *Nano letters*, vol. 14, no. 2, pp. 1080–1084, 2014.

- [33] S. Lim, C. S. Yoon, and J. Cho, “Synthesis of nanowire and hollow lifepo₄ cathodes for high-performance lithium batteries,” *Chemistry of Materials*, vol. 20, no. 14, pp. 4560–4564, 2008.
- [34] N. Choudhary, C. Li, H.-S. Chung, J. Moore, J. Thomas, and Y. Jung, “High-performance one-body core/shell nanowire supercapacitor enabled by conformal growth of capacitive 2d ws₂ layers,” *ACS nano*, vol. 10, no. 12, pp. 10726–10735, 2016.
- [35] Z. Chen, D. Yu, W. Xiong, P. Liu, Y. Liu, and L. Dai, “Graphene-based nanowire supercapacitors,” *Langmuir*, vol. 30, no. 12, pp. 3567–3571, 2014.
- [36] H. Jiang, J. Ma, and C. Li, “Hierarchical porous nico 2 o 4 nanowires for high-rate supercapacitors,” *Chemical communications*, vol. 48, no. 37, pp. 4465–4467, 2012.
- [37] Z. Chen, V. Augustyn, J. Wen, Y. Zhang, M. Shen, B. Dunn, and Y. Lu, “High-performance supercapacitors based on intertwined cnt/v2o₅ nanowire nanocomposites,” *Advanced materials*, vol. 23, no. 6, pp. 791–795, 2011.
- [38] L. Hu, H. Wu, S. S. Hong, L. Cui, J. R. McDonough, S. Bohy, and Y. Cui, “Si nanoparticle-decorated si nanowire networks for li-ion battery anodes,” *Chemical Communications*, vol. 47, no. 1, pp. 367–369, 2011.
- [39] X. Li, J.-H. Cho, N. Li, Y. Zhang, D. Williams, S. A. Dayeh, and S. Picraux, “Carbon nanotube-enhanced growth of silicon nanowires as an anode for high-performance lithium-ion batteries,” *Advanced Energy Materials*, vol. 2, no. 1, pp. 87–93, 2012.
- [40] J. W. Choi, L. Hu, L. Cui, J. R. McDonough, and Y. Cui, “Metal current collector-free freestanding silicon–carbon 1d nanocomposites for ultralight anodes in lithium ion batteries,” *Journal of Power Sources*, vol. 195, no. 24, pp. 8311–8316, 2010.
- [41] E. Peled, F. Patolsky, D. Golodnitsky, K. Freedman, G. Davidi, and D. Schneier, “Tissue-like silicon nanowires-based three-dimensional anodes for high-capacity lithium ion batteries,” *Nano letters*, vol. 15, no. 6, pp. 3907–3916, 2015.
- [42] H. Kim and J. Cho, “Superior lithium electroactive mesoporous si@ carbon core- shell nanowires for lithium battery anode material,” *Nano letters*, vol. 8, no. 11, pp. 3688–3691, 2008.
- [43] Y.-D. Ko, J.-G. Kang, G.-H. Lee, J.-G. Park, K.-S. Park, Y.-H. Jin, and D.-W. Kim, “Sn-induced low-temperature growth of ge nanowire electrodes with a large lithium storage capacity,” *Nanoscale*, vol. 3, no. 8, pp. 3371–3375, 2011.
- [44] F. Jiao, K. M. Shaju, and P. G. Bruce, “Synthesis of nanowire and mesoporous low-temperature licoo₂ by a post-templating reaction,” *Angewandte Chemie International Edition*, vol. 44, no. 40, pp. 6550–6553, 2005.
- [45] H. Xia, Y. Wan, W. Assenmacher, W. Mader, G. Yuan, and L. Lu, “Facile synthesis of chain-like licoo 2 nanowire arrays as three-dimensional cathode for microbatteries,” *NPG Asia Materials*, vol. 6, no. 9, pp. e126–e126, 2014.
- [46] M. Raghuveer, P. Ganesan, J. D’Arcy-Gall, G. Ramanath, M. Marshall, and I. Petrov, “Nanomachining carbon nanotubes with ion beams,” *Applied physics letters*, vol. 84, no. 22, pp. 4484–4486, 2004.
- [47] L.-F. Chen, Y. Lu, L. Yu, and X. W. D. Lou, “Designed formation of hollow particle-based nitrogen-doped carbon nanofibers for high-performance supercapacitors,” *Energy & Environmental Science*, vol. 10, no. 8, pp. 1777–1783, 2017.
- [48] H. Xia, C. Hong, X. Shi, B. Li, G. Yuan, Q. Yao, and J. Xie, “Hierarchical heterostructures of ag nanoparticles decorated mno 2 nanowires as promising electrodes for supercapacitors,” *Journal of Materials Chemistry A*, vol. 3, no. 3, pp. 1216–1221, 2015.
- [49] S. Dhal, S. Chatterjee, S. Sarkar, L. C. Tribedi, R. Bapat, and P. Ayyub, “Nano-welding and junction formation in hydrogen titanate nanowires by low-energy nitrogen ion irradiation,” *Nanotechnology*, vol. 26, no. 23, p. 235601, 2015.

- [50] S. Dhal, P. Das, M. K. Rajbhar, W. Möller, S. Chatterjee, N. Ramgir, and S. Chatterjee, “Superior electrical conduction of a water repelling 3d interconnected nano-network,” *Journal of Materials Chemistry C*, vol. 6, no. 8, pp. 1951–1958, 2018.
- [51] F. Banhart and P. M. Ajayan, “Carbon onions as nanoscopic pressure cells for diamond formation,” *Nature*, vol. 382, no. 6590, pp. 433–435, 1996.
- [52] A. Hashimoto, K. Suenaga, A. Gloter, K. Urita, and S. Iijima, “Direct evidence for atomic defects in graphene layers,” *Nature*, vol. 430, no. 7002, pp. 870–873, 2004.
- [53] B. Peng, M. Locascio, P. Zapol, S. Li, S. L. Mielke, G. C. Schatz, and H. D. Espinosa, “Measurements of near-ultimate strength for multiwalled carbon nanotubes and irradiation-induced crosslinking improvements,” *Nature nanotechnology*, vol. 3, no. 10, p. 626, 2008.
- [54] B. W. Smith, M. Monthioux, and D. E. Luzzi, “Encapsulated c 60 in carbon nanotubes,” *Nature*, vol. 396, no. 6709, pp. 323–324, 1998.
- [55] A. Kis, G. Csanyi, J.-P. Salvetat, T.-N. Lee, E. Couteau, A. Kulik, W. Benoit, J. Brugger, and L. Forro, “Reinforcement of single-walled carbon nanotube bundles by intertube bridging,” *Nature materials*, vol. 3, no. 3, pp. 153–157, 2004.
- [56] C. Gómez-Navarro, P. J. De Pablo, J. Gómez-Herrero, B. Biel, F. Garcia-Vidal, A. Rubio, and F. Flores, “Tuning the conductance of single-walled carbon nanotubes by ion irradiation in the anderson localization regime,” *Nature materials*, vol. 4, no. 7, pp. 534–539, 2005.
- [57] M. Terrones, H. Terrones, F. Banhart, J.-C. Charlier, and P. Ajayan, “Coalescence of single-walled carbon nanotubes,” *Science*, vol. 288, no. 5469, pp. 1226–1229, 2000.
- [58] Ç. Ö. Girit, J. C. Meyer, R. Erni, M. D. Rossell, C. Kisielowski, L. Yang, C.-H. Park, M. Crommie, M. L. Cohen, S. G. Louie, *et al.*, “Graphene at the edge: stability and dynamics,” *science*, vol. 323, no. 5922, pp. 1705–1708, 2009.
- [59] D. Ugarte, “Curling and closure of graphitic networks under electron-beam irradiation,” *Nature*, vol. 359, no. 6397, pp. 707–709, 1992.
- [60] A. Krasheninnikov and F. Banhart, “Engineering of nanostructured carbon materials with electron or ion beams,” *Nature materials*, vol. 6, no. 10, pp. 723–733, 2007.
- [61] J. H. Warner, M. H. Rümmeli, L. Ge, T. Gemming, B. Montanari, N. M. Harrison, B. Büchner, and G. A. D. Briggs, “Structural transformations in graphene studied with high spatial and temporal resolution,” *Nature nanotechnology*, vol. 4, no. 8, p. 500, 2009.
- [62] H. Stahl, J. Appenzeller, R. Martel, P. Avouris, and B. Lengeler, “Intertube coupling in ropes of single-wall carbon nanotubes,” *Physical Review Letters*, vol. 85, no. 24, p. 5186, 2000.
- [63] B. Wei, J. D’Arcy-Gall, P. Ajayan, and G. Ramanath, “Tailoring structure and electrical properties of carbon nanotubes using kilo-electron-volt ions,” *Applied Physics Letters*, vol. 83, no. 17, pp. 3581–3583, 2003.
- [64] P. Das, M. K. Rajbhar, R. G. Elliman, W. Möller, S. Facsko, and S. Chatterjee, “Nanoscale modification of one-dimensional single-crystalline cuprous oxide,” *Nanotechnology*, vol. 30, no. 36, p. 365304, 2019.
- [65] S. Talapatra, P. Ganesan, T. Kim, R. Vajtai, M. Huang, M. Shima, G. Ramanath, D. Srivastava, S. Deevi, and P. Ajayan, “Irradiation-induced magnetism in carbon nanostructures,” *Physical review letters*, vol. 95, no. 9, p. 097201, 2005.
- [66] P. Esquinazi, D. Spemann, R. Höhne, A. Setzer, K.-H. Han, and T. Butz, “Induced magnetic ordering by proton irradiation in graphite,” *Physical review letters*, vol. 91, no. 22, p. 227201, 2003.
- [67] W. Mickelson, S. Aloni, W.-Q. Han, J. Cumings, and A. Zettl, “Packing c60 in boron nitride nanotubes,” *Science*, vol. 300, no. 5618, pp. 467–469, 2003.

- [68] M. Terrones, F. Banhart, N. Grobert, J.-C. Charlier, H. Terrones, and P. Ajayan, “Molecular junctions by joining single-walled carbon nanotubes,” *Physical review letters*, vol. 89, no. 7, p. 075505, 2002.
- [69] B. Ni, R. Andrews, D. Jacques, D. Qian, M. B. Wijesundara, Y. Choi, L. Hanley, and S. B. Sinnott, “A combined computational and experimental study of ion-beam modification of carbon nanotube bundles,” *The Journal of Physical Chemistry B*, vol. 105, no. 51, pp. 12719–12725, 2001.
- [70] C. Miko, M. Milas, J. W. Seo, E. Couteau, N. Barišić, R. Gaal, and L. Forró, “Effect of electron irradiation on the electrical properties of fibers of aligned single-walled carbon nanotubes,” *Applied physics letters*, vol. 83, no. 22, pp. 4622–4624, 2003.
- [71] Z. Ni, Q. Li, D. Zhu, and J. Gong, “Fabrication of carbon nanowire networks by si ion beam irradiation,” *Applied physics letters*, vol. 89, no. 5, p. 053107, 2006.
- [72] P. Ajayan, V. Ravikumar, and J.-C. Charlier, “Surface reconstructions and dimensional changes in single-walled carbon nanotubes,” *Physical Review Letters*, vol. 81, no. 7, p. 1437, 1998.
- [73] Z. Wang, L. Yu, W. Zhang, Y. Ding, Y. Li, J. Han, Z. Zhu, H. Xu, G. He, Y. Chen, *et al.*, “Amorphous molecular junctions produced by ion irradiation on carbon nanotubes,” *Physics Letters A*, vol. 324, no. 4, pp. 321–325, 2004.
- [74] A. Ishaq, Z. Ni, L. Yan, J. Gong, and D. Zhu, “Constructing carbon nanotube junctions by ar ion beam irradiation,” *Radiation Physics and Chemistry*, vol. 79, no. 6, pp. 687–691, 2010.
- [75] A. Rahman, “Correlations in the motion of atoms in liquid argon,” *Physical review*, vol. 136, no. 2A, p. A405, 1964.
- [76] A. Cao, “Molecular dynamics simulation study on heat transport in monolayer graphene sheet with various geometries,” *Journal of Applied Physics*, vol. 111, no. 8, p. 083528, 2012.
- [77] Y.-Y. Zhang, Q.-X. Pei, J.-W. Jiang, N. Wei, and Y.-W. Zhang, “Thermal conductivities of single-and multi-layer phosphorene: a molecular dynamics study,” *Nanoscale*, vol. 8, no. 1, pp. 483–491, 2016.
- [78] Z. Fan, L. F. C. Pereira, P. Hirvonen, M. M. Ervasti, K. R. Elder, D. Donadio, T. Ala-Nissila, and A. Harju, “Thermal conductivity decomposition in two-dimensional materials: Application to graphene,” *Physical Review B*, vol. 95, no. 14, p. 144309, 2017.
- [79] W.-R. Zhong, M.-P. Zhang, B.-Q. Ai, and D.-Q. Zheng, “Chirality and thickness-dependent thermal conductivity of few-layer graphene: A molecular dynamics study,” *Applied Physics Letters*, vol. 98, no. 11, p. 113107, 2011.
- [80] A. N. Camden, S. A. Barr, and R. J. Berry, “Simulations of peptide-graphene interactions in explicit water,” *The Journal of Physical Chemistry B*, vol. 117, no. 37, pp. 10691–10697, 2013.
- [81] B. Akdim, R. Pachter, S. S. Kim, R. R. Naik, T. R. Walsh, S. Trohalaki, G. Hong, Z. Kuang, and B. L. Farmer, “Electronic properties of a graphene device with peptide adsorption: insight from simulation,” *ACS applied materials & interfaces*, vol. 5, no. 15, pp. 7470–7477, 2013.
- [82] S. M. Tomásio and T. R. Walsh, “Modeling the binding affinity of peptides for graphitic surfaces. influences of aromatic content and interfacial shape,” *The Journal of Physical Chemistry C*, vol. 113, no. 20, pp. 8778–8785, 2009.
- [83] L. Baweja, K. Balamurugan, V. Subramanian, and A. Dhawan, “Hydration patterns of graphene-based nanomaterials (gbnms) play a major role in the stability of a helical protein: a molecular dynamics simulation study,” *Langmuir*, vol. 29, no. 46, pp. 14230–14238, 2013.
- [84] Y. Jing, Q. Meng, and W. Zhao, “Molecular dynamics simulations of the tensile and melting behaviours of silicon nanowires,” *Physica E: Low-dimensional Systems and Nanostructures*, vol. 41, no. 4, pp. 685–689, 2009.

- [85] A. Alavi, K. Mirabbaszadeh, P. Nayebi, and E. Zaminpayma, "Molecular dynamics simulation of mechanical properties of ni-al nanowires," *Computational Materials Science*, vol. 50, no. 1, pp. 10–14, 2010.
- [86] S. Joshi, K. Pandey, S. K. Singh, and S. Dubey, "Molecular dynamics simulations of deformation behaviour of gold nanowires," *Journal of Nanotechnology*, vol. 2019, 2019.
- [87] L. Dai, W. Cheong, C. Sow, C. Lim, and V. Tan, "Molecular dynamics simulation of zno nanowires: size effects, defects, and super ductility," *Langmuir*, vol. 26, no. 2, pp. 1165–1171, 2009.
- [88] L. Verlet, "Computer" experiments" on classical fluids. i. thermodynamical properties of lennard-jones molecules," *Physical review*, vol. 159, no. 1, p. 98, 1967.
- [89] H. J. Berendsen, J. v. Postma, W. F. van Gunsteren, A. DiNola, and J. R. Haak, "Molecular dynamics with coupling to an external bath," *The Journal of chemical physics*, vol. 81, no. 8, pp. 3684–3690, 1984.
- [90] H. C. Andersen, "Molecular dynamics simulations at constant pressure and/or temperature," *The Journal of chemical physics*, vol. 72, no. 4, pp. 2384–2393, 1980.
- [91] S. Nosé, "A unified formulation of the constant temperature molecular dynamics methods," *The Journal of chemical physics*, vol. 81, no. 1, pp. 511–519, 1984.
- [92] S. Nosé, "A molecular dynamics method for simulations in the canonical ensemble," *Molecular physics*, vol. 52, no. 2, pp. 255–268, 1984.
- [93] W. G. Hoover, "Canonical dynamics: Equilibrium phase-space distributions," *Physical review A*, vol. 31, no. 3, p. 1695, 1985.
- [94] S. Plimpton, "Fast parallel algorithms for short-range molecular dynamics," *Journal of computational physics*, vol. 117, no. 1, pp. 1–19, 1995.
- [95] W. Humphrey, A. Dalke, and K. Schulten, "VMD – Visual Molecular Dynamics," *Journal of Molecular Graphics*, vol. 14, pp. 33–38, 1996.
- [96] M. Cubillos, M. P. Alba, A. Bermúdez, M. Trujillo, and M. E. Patarroyo, "Plasmodium falciparum sera protein peptide analogues having short helical regions induce protection against malaria," *Biochimie*, vol. 85, no. 7, pp. 651–657, 2003.
- [97] S. Vijay-Kumar, C. E. Bugg, and W. J. Cook, "Structure of ubiquitin refined at 1.8 åresolution," *Journal of molecular biology*, vol. 194, no. 3, pp. 531–544, 1987.
- [98] H. M. Berman, J. Westbrook, Z. Feng, G. Gilliland, T. Bhat, H. Weissig, I. Shindyalov, and P. Bourne, "The protein data bank," *Nucleic Acids Res*, vol. 28, pp. 235–242, 2000.
- [99] D.A. Case, I.Y. Ben-Shalom, S.R. Brozell, D.S. Cerutti, T.E. Cheatham, III, V.W.D. Cruzeiro, T.A. Darden, R.E. Duke, D. Ghoreishi, M.K. Gilson, H. Gohlke, A.W. Goetz, D. Greene, R Harris, N. Homeyer, S. Izadi, A. Kovalenko, T. Kurtzman, T.S. Lee, S. LeGrand, P. Li, C. Lin, J. Liu, T. Luchko, R. Luo, D.J. Mermelstein, K.M. Merz, Y. Miao, G. Monard, C. Nguyen, H. Nguyen, I. Omelyan, A. Onufriev, F. Pan, R. Qi, D.R. Roe, A. Roitberg, C. Saggi, S. Schott-Verdugo, J. Shen, C.L. Simmerling, J. Smith, R. Salomon-Ferrer, J. Swails, R.C. Walker, J. Wang, H. Wei, R.M. Wolf, X. Wu, L. Xiao, D.M. York and P.A. Kollman, "Amber 2018," 2018.
- [100] F. K. Schwab and C. Denniston, "Reaction and characterisation of a two-stage thermoset using molecular dynamics," *Polymer Chemistry*, vol. 10, no. 32, pp. 4413–4427, 2019.